

{Co₄O₄} and {Co_xNi_{4-x}O₄} cubane water oxidation catalysts as surface cut-outs of cobalt oxides

Fangyuan Song, René Moré, Mauro Schilling, Grigory Smolentsev, Nicolo Azzaroli, Thomas Fox,
Sandra Lubner, and Greta R. Patzke*

Supporting Information

Analytical characterization.	S3
Experimental section and methods.	
• Materials	S4
• Synthesis of Co _x Ni _{4-x} O ₄ -dpk (0 ≤ x ≤ 4), Co ₄ O ₄ -dpk (OAc-d ₃), mono-Co-dpk, and [Ru(bpy) ₃](ClO ₄) ₃ .	S4
• Analytical data of Co ₄ O ₄ -dpk, Co _x Ni _{4-x} O ₄ -dpk, and Ni ₄ O ₄ -dpk.	S5
• Photocatalytic water oxidation	S5
• Recycling tests	S5
• ¹⁸ O labeling experiments	S6
• pH-dependent UV/vis titrations	S6
• Cyclic voltammetry	S6
• Acetate ligand exchange study	S6
• Ligation study of {Co ₂ O ₂ (OH) ₂ }	S6
• X-ray absorption spectroscopy	S6
• Chemical water oxidation with Co ₄ O ₄ -dpk	S7
• Crystallographic information and structural description of Co ₄ O ₄ -dpk	S7
Table S1. Crystallographic and structural refinement data of [Co ₄ (dpv{OH}O) ₄ (OAc) ₂ (H ₂ O) ₂](ClO ₄) ₂ .	S8
Table S2. Selected bond lengths and distances of Co ₄ O ₄ -dpk.	S8
Table S3. Bond valence sum (BVS) calculation for Co in Co ₄ O ₄ -dpk.	S9
Figure S1. ORTEP and structural representations of Co ₄ O ₄ -dpk.	S9
Figure S2. TG characterizations of Co ₄ O ₄ -dpk, the Co _x Ni _{4-x} O ₄ -dpk series, and Ni ₄ O ₄ -dpk.	S10
Figure S3. HR-ESI-MS spectrum of Co ₄ O ₄ -dpk.	S10
Figure S4. FT-IR spectra of Co ₄ O ₄ -dpk, Ni ₄ O ₄ -dpk, and the Co _x Ni _{4-x} O ₄ -dpk series.	S11
Figure S5. Time dependent UV/vis spectra of Co ₄ O ₄ -dpk in pH 8.5, 80 mM borate buffer solution.	S11
Figure S6. pH dependent UV/vis spectra of Co ₄ O ₄ -dpk and the corresponding titration curve.	S12
Figure S7. Cyclic voltammograms of Co ₄ O ₄ -dpk in the pH range of 4-11.	S13
Figure S8. Cyclic voltammograms of 1 mM Co ₄ O ₄ -dpk in the pH range of 7.0-9.0.	S13
Figure S9. Pourbaix diagram of Co ₄ O ₄ -dpk in the pH range of 7 - 9.	S14
Figure S10. Cyclic voltammograms of 1 mM Co ₄ O ₄ -dpk and 1 mM [Ru(bpy) ₃]Cl ₂ .	S14
Figure S11. PXRD pattern of Co ₄ O ₄ -dpk(OAc-d ₃).	S15
Figure S12. ¹ H NMR spectrum of Co ₄ O ₄ -dpk in CD ₃ CN.	S15
Figure S13. ¹ H NMR spectrum of Co ₄ O ₄ -dpk immediately after D ₂ O addition and after an interval of 30 h.	S16
Figure S14. Clark electrode kinetics of various concentrations of Co ₄ O ₄ -dpk.	S16
Figure S15. Photocatalytic water oxidation of Co ₄ O ₄ -dpk in different borate buffer concentrations.	S17
Figure S16. Clark electrode kinetics: Co ₄ O ₄ -dpk, [Co ₄ (dpv{OH}O) ₄ (OAc) ₃ (H ₂ O)](ClO ₄), mono-Co-dpk.	S17
Figure S17. Photocatalytic water oxidation performance of Co ₄ O ₄ -dpk, NaClO ₄ , and references.	S18
Table S4. Photocatalytic water oxidation performance with different Co ₄ O ₄ -dpk concentrations.	S18
Table S5. Photocatalytic water oxidation performance of Co ₄ O ₄ -dpk in different buffer solutions.	S18
Table S6. Photocatalytic water oxidation of Co ₄ O ₄ -dpk in different borate buffer concentrations.	S19
Figure S18. PXRD pattern and FT-IR spectra of Co ₄ O ₄ -dpk synthesized from borate buffer.	S19

Figure S19. Time-dependent FT-IR spectra of Co₄O₄-dpk in pH 8.5, 80 mM borate buffer.	S19
Figure S20. Clark electrode kinetics of activity recycling tests of Co₄O₄-dpk vs. Co(OAc) ₂ .	S20
Figure S21. Clark electrode kinetics of filtered post-catalytic solutions with Co₄O₄-dpk vs. Co(OAc) ₂ .	S20
Figure S22. DLS measurement of the post-catalytic reaction solution of Co₄O₄-dpk .	S21
Figure S23. Clark electrode kinetics of Chelex tests for Co₄O₄-dpk vs. Co(OAc) ₂ .	S21
Figure S24. FT-IR spectra of Co₄O₄-dpk in formamide and formamide containing phosphate.	S22
Table S7. EXAFS fit results for Co₄O₄-dpk after photocatalytic oxygen evolution.	S22
Figure S25. Kinetics of Co₄O₄-dpk catalyzed chemical water oxidation with [Ru(bpy) ₃](ClO ₄) ₃ .	S23
Figure S26. Kinetics of Co₄O₄-dpk catalyzed chemical water oxidation with 1 - 5 eq of [Ru(bpy) ₃](ClO ₄) ₃ .	S23
Figure S27. UV/vis kinetics of Co₄O₄-dpk catalyzed chemical water oxidation with [Ru(bpy) ₃](ClO ₄) ₃ .	S24
Figure S28. ¹ H NMR spectra of [(NH ₃) ₄ Co(III)sal]Cl and [(NH ₃) ₄ Co(IV)sal-NO ₂]ClNO ₃ .	S24
Figure S29. Comparison of the edge position and white line for different cobalt containing samples.	S25
Figure S30. Normalized XANES spectra of cobalt amino salicylic acid complexes and 1 st derivative.	S25
Figure S31. White line position of XANES measurement of 100 μM Co₄O₄-dpk in borate buffer.	S26
Figure S32. Cobalt K-edge XANES spectra of Co₄O₄-dpk oxidized by [Ru(bpy) ₃](ClO ₄) ₃ at 40 K.	S26
Figure S33. Mass spectra of Co₄O₄-dpk assisted O ₂ evolution with H ₂ ¹⁶ O vs. H ₂ ¹⁸ O containing borate buffer.	S27
Figure S34. GC data of Co₄O₄-dpk catalyzed ³² O ₂ , ³⁴ O ₂ , and ³⁶ O ₂ from a H ₂ ¹⁶ O containing borate buffer.	S27
Figure S35. GC data of Co₄O₄-dpk catalyzed ³² O ₂ , ³⁴ O ₂ , and ³⁶ O ₂ from a H ₂ ¹⁸ O containing borate buffer.	S28
Figure S36. Co₄O₄-dpk assisted ³² , ³⁴ , and ³⁶ O ₂ evolution from H ₂ ¹⁸ O containing borate buffer.	S28
Current research survey and Table S8: Mixed Co/Ni-containing water oxidation catalysts.	S29
Figure S37. Syntheses of Co₄O₄-dpk , Co_xNi_{4-x}O₄-dpk series, and Ni₄O₄-dpk .	S31
Figure S38. Time dependent UV/vis spectra of Co_{2.65}Ni_{1.35}O₄-dpk in pH 8.5 borate buffer solution.	S31
Figure S39. Time dependent UV/vis spectra of Co_{2.05}Ni_{1.95}O₄-dpk in pH 8.5 borate buffer solution.	S32
Figure S40. Time dependent UV/vis spectra of Co_{1.15}Ni_{2.85}O₄-dpk in pH 8.5 borate buffer solution.	S32
Figure S41. Time dependent UV/vis spectra of Ni₄O₄-dpk cubane in pH 8.5 borate buffer solution.	S33
Figure S42. Compared HR-ESI-MS spectra of Co₄O₄-dpk , Ni₄O₄-dpk , and Co_{1.15}Ni_{2.85}O₄-dpk .	S33
Figure S43. Calculated MS spectrum of Co_{1.15}Ni_{2.85}O₄-dpk in the <i>m/z</i> range of 577.0-584.5.	S34
Table S9. Photocatalytic water oxidation performance of Co₄O₄-dpk and the Co_xNi_{4-x}O₄-dpk series.	S34
Figure S44. Photocatalytic water oxidation performance of Co₄O₄-dpk and the Co_xNi_{4-x}O₄-dpk series.	S34
Figure S45. Mass spectra of Co_{2.65}Ni_{1.35}O₄-dpk catalyzed O ₂ evolution with H ₂ ¹⁶ O vs. H ₂ ¹⁸ O-borate buffer.	S35
Figure S46. GC data of Co_{2.65}Ni_{1.35}O₄-dpk catalyzed ³² , ³⁴ and ³⁶ O ₂ evolution from a H ₂ ¹⁶ O-borate buffer.	S35
Figure S47. GC data of Co_{2.65}Ni_{1.35}O₄-dpk catalyzed ³² , ³⁴ and ³⁶ O ₂ evolution from a H ₂ ¹⁸ O-borate buffer.	S36
Figure S48. Representative Co_{2.65}Ni_{1.35}O₄-dpk assisted ³² , ³⁴ and ³⁶ O ₂ evolution in H ₂ ¹⁸ O-borate buffer.	S36
Figure S49. pH dependent UV/vis spectra of Ni₄O₄-dpk with plot of the absorbance at 389 nm.	S37
Computational Settings.	S38
Table S10. Description of oxygen-oxygen radial distribution function.	S38
Figure S50. Radial distribution function of water molecules in the simulation box of the neutral cubane.	S39
Table S11. Structure optimizations of Co₄O₄-dpk .	S39
Figure S51. Evolution of volume enclosed by the cubane cage of Co₄O₄-dpk during the DFT-MD run.	S40
Figure S52. Clark electrode kinetics of water oxidation catalyzed by Co₄O₄-dpk and mono-Co-dpk .	S41
Figure S53. TOF per Co center for the reactions of Figure S52 .	S41
Figure S54. Tentative evaluation of mono-Co-dpk and Co₄O₄-dpk for first order kinetics.	S42

Analytical characterizations.

Thermogravimetric (TG) analyses were performed on a Netzsch STA Jupiter 449 F3 TGA in the temperature range 298 to 1173 K with a heating rate of 10 K min⁻¹ in N₂ atmosphere in an Al₂O₃ crucible.

Powder X-ray diffraction (PXRD) patterns were recorded on a STOE STADI P diffractometer (transmission mode, Ge monochromator) with Mo K_α radiation.

Attenuated total reflectance Fourier-transform infrared (ATR-FT-IR) spectra were recorded on a Bruker Vertex 70 spectrometer equipped with a Platinum ATR accessory containing a diamond crystal.

Operando FT-IR spectra were recorded on a ReactIR iC 10 FT-IR spectrometer (METTLER TOLEDO) equipped with a Silver Halide (AgX) DSub AgX FiberConduit probe (METTLER TOLEDO).

UV/vis spectra were recorded on a Lambda 650 S Perkin Elmer UV/visible spectrometer in the range of 300-800 nm using a Quartz SUPRASIL precision cell (10 mm).

Dynamic light scattering (DLS) measurements were carried out with a Zetasizer Nano 3600 instrument (Malvern Instruments Ltd.).

High-resolution electrospray mass spectra (HR-ESI-MS) were recorded on a Bruker maXis QTOFMS instrument (Bruker Daltonics GmbH, Bremen, Germany). The samples were dissolved in MeOH and analyzed via continuous flow injection at 3 μL/min. The mass spectrometer was calibrated between m/z 50 and 3000 using a Fluka electrospray calibration solution (Sigma-Aldrich, Buchs, Switzerland) at a resolution of 20'000 and a mass accuracy below 2 ppm.

NMR measurements were performed on a BRUKER AV3-500 spectrometer (500.25 MHz ¹H frequency), and the longitudinal relaxation times (T₁) were determined with the inversion recovery method.

Experimental section.

Materials

All chemicals and solvents were purchased from commercial suppliers: [Ru(bpy)₃]Cl₂·6H₂O (Sigma-Aldrich, 99.95%), Na₂S₂O₈ (Sigma-Aldrich, ≥99.0%), Co(OAc)₂·4H₂O (Sigma-Aldrich, ≥99.0%), Ni(OAc)₂·4H₂O (Sigma-Aldrich, ≥99.0%), NaClO₄ (Sigma-Aldrich, ≥98.0%), di(2-pyridyl) ketone (Sigma-Aldrich, 99%), Co(ClO₄)₂·6H₂O (Sigma-Aldrich, ≥99.0%), Chelex® 100 sodium form (Sigma-Aldrich, 50-100 mesh), NaOAc-d₃ (Sigma-Aldrich, 99 at% D), D₃CCOOD (Sigma-Aldrich, 99.5 at% D), D₂O (Sigma-Aldrich, 99.9 at% D), H₂¹⁸O (Sigma-Aldrich, 97 at% ¹⁸O), CD₃CN (Sigma-Aldrich, 99.8 at% D), formamide (Fluka, ≥99.0%).

Ultrapure water was produced from a Barnstead GenPure Pro Water Purification System with an electric conductivity of 0.055 μS/cm (Thermo Scientific).

Synthesis of [Co₄(dpy{OH}O)₄(OAc)₂(H₂O)₂](ClO₄)₂ (Co₄O₄-dpk)

Co₄O₄-dpk was obtained from a modified and optimized literature protocol by Perlepes *et al.* for **Ni₄O₄-dpk**.¹ 0.2 g Co(OAc)₂·4H₂O (0.8 mmol) and 0.147 g NaClO₄ (1.2 mmol) were both dissolved in 3 mL H₂O. 3 mL aqueous solution of 0.0736 g dpk (0.4 mmol) was added to the above solution dropwise under stirring. The solution was filtered to keep the filtrate for crystallization at room temperature. Violet crystals of **Co₄O₄-dpk** were obtained over night.

The above procedure was slightly modified for the synthesis of **Co₄O₄-dpk** in borate buffer solution. Instead of water, a pH 8.5 borate buffer (0.5 M) was used for mixing the starting materials (0.1 g Co(OAc)₂·4H₂O (0.4 mmol), 0.27 g NaClO₄ (2.2 mmol), and 0.0736 g dpk (0.4 mmol)).

Synthesis of [Co₄(dpy{OH}O)₄(OAc-d₃)₂(H₂O)₂](ClO₄)₂ (Co₄O₄-dpk(OAc-d₃))

Co₄O₄-dpk(OAc-d₃) was obtained from a modification of the above synthetic procedure for **Co₄O₄-dpk** by starting from 0.293 g (0.8 mmol) Co(ClO₄)₂·4H₂O and 0.132 g NaOAc-d₃ (1.6 mmol).

Synthesis of [Co_xNi_{4-x}(dpy{OH}O)₄(OAc)₂(H₂O)₂](ClO₄)₂ (Co_xNi_{4-x}O₄-dpk)

The entire series of heterometallic Co-Ni mixed cubanes was obtained from the synthetic procedure of **Co₄O₄-dpk** by applying mixtures of Co(OAc)₂·4H₂O and Ni(OAc)₂·4H₂O with the following ratios: **Co_{2.80}Ni_{1.20}O₄-dpk**, 0.64 mmol Co(OAc)₂·4H₂O + 0.16 mmol Ni(OAc)₂·4H₂O; **Co_{2.65}Ni_{1.35}O₄-dpk**, 0.6 mmol Co(OAc)₂·4H₂O + 0.2 mmol Ni(OAc)₂·4H₂O; **Co_{2.05}Ni_{1.95}O₄-dpk**, 0.4 mmol Co(OAc)₂·4H₂O + 0.4 mmol Ni(OAc)₂·4H₂O; **Co_{1.15}Ni_{2.85}O₄-dpk**, 0.2 mmol Co(OAc)₂·4H₂O + 0.6 mmol Ni(OAc)₂·4H₂O. Crystals were obtained within 4 to 7 d, depending on the increasing Ni contents.

Synthesis of [Ni₄(dpy{OH}O)₄(OAc)₂(H₂O)₂](ClO₄)₂ (Ni₄O₄-dpk)

The synthesis of **Ni₄O₄-dpk** is similar to the above literature protocol,¹ starting from 0.2 g Ni(OAc)₂·4H₂O (0.8 mmol) and a larger amount of NaClO₄ (0.245 g, 2.0 mmol). Green crystals were obtained within 7 d.

Synthesis of [Co^{III}(dpy{OH}O)₂]ClO₄ (mono-Co-dpk).

[Co^{III}(dpy{OH}O)₂]ClO₄ was synthesized according the reported procedure by using Co(ClO₄)₂·6H₂O instead of CoCl₂·6H₂O.²

Synthesis of [Ru(bpy)₃](ClO₄)₃

PbO₂ was added to 10 mL of 0.5 mM H₂SO₄ containing 0.3 g [Ru(bpy)₃]Cl₂ until the liquid phase turned to green. The reaction was completed in an ice bath under stirring for 10 min. A dark green solution was obtained by filtering off PbO₂. 2 M HClO₄ was dropwise added into above green solution until the formation of a green precipitate set in, and [Ru(bpy)₃](ClO₄)₃ was obtained from filtering as a green solid.

(1) Efthymiou, C. G.; Raptopoulou, C. P.; Terzis, A.; Boča, R.; Korabic, M.; Mrozinski, J.; Perlepes, S. P.; Bakalbassis, E. G. *Eur. J. Inorg. Chem.* **2006**, 2006, 2236–2252.

(2) Zhao, Y.; Lin, J.; Liu, Y.; Ma, B.; Ding, Y.; Chen, M. *Chem. Commun.* **2015**, 51, 17309–17312.

Non-metal elemental analysis of **Co₄O₄-dpk** (C₄₈H₄₆Cl₂Co₄N₈O₂₂): calc. (%) C, 41.36; H, 3.30; N, 8.04; Cl, 5.10; found (%) C, 40.90; H, 3.33; N, 7.87; Cl, 5.19. (Co = 58.93)

Non-metal elemental analysis of **Co_{2.80}Ni_{1.20}O₄-dpk** (C₄₈H₄₆Cl₂Co_xNi_{4-x}N₈O₂₂): calc. (%) C, 41.35; H, 3.30; N, 8.04; Cl, 5.10; found (%) C, 40.94; H, 3.35; N, 7.95; Cl, 5.01. (Co = Ni = 59)

Non-metal elemental analysis of **Co_{2.65}Ni_{1.35}O₄-dpk** (C₄₈H₄₆Cl₂Co_{x2}Ni_{4-x2}N₈O₂₂): calc. (%) C, 41.35; H, 3.30; N, 8.04; Cl, 5.10; found (%) C, 40.87; H, 3.37; N, 8.17; Cl, 5.22. (Co = Ni = 59)

Non-metal elemental analysis of **Co_{2.05}Ni_{1.95}O₄-dpk** (C₄₈H₄₆Cl₂Co_{x3}Ni_{4-x3}N₈O₂₂): calc. (%) C, 41.35; H, 3.30; N, 8.04; Cl, 5.10; found (%) C, 40.92; H, 3.34; N, 7.90; Cl, 5.17. (Co = Ni = 59)

Non-metal elemental analysis of **Co_{1.15}Ni_{2.85}O₄-dpk** (C₄₈H₄₆Cl₂Co_{x4}Ni_{4-x4}N₈O₂₂): calc. (%) C, 41.35; H, 3.30; N, 8.04; Cl, 5.10; found (%) C, 40.95; H, 3.37; N, 7.92; Cl, 5.25. (Co = Ni = 59)

Non-metal elemental analysis of **Ni₄O₄-dpk** (C₄₈H₄₆Cl₂Ni₄N₈O₂₂): calc. (%) C, 41.39; H, 3.30; N, 8.05; Cl, 5.10; found (%) C, 41.02, H, 3.39; N, 8.22; Cl, 4.98. (Ni = 58.69)

ICP-MS elemental analysis of **Co₄O₄-dpk** (C₄₈H₄₆Cl₂Co₄N₈O₂₂): calc. (%) Co, 16.9; found (%) Co, 16.9.

ICP-MS elemental analysis of **Co_{2.80}Ni_{1.20}O₄-dpk** (C₄₈H₄₆Cl₂Co_xNi_{4-x}N₈O₂₂): calc. (%) Co + Ni, 16.9; found (%) Co, 11.7; Ni, 5.04.

ICP-MS elemental analysis of **Co_{2.65}Ni_{1.35}O₄-dpk** (C₄₈H₄₆Cl₂Co_xNi_{4-x}N₈O₂₂): calc. (%) Co + Ni, 16.9; found (%) Co, 11.1; Ni, 5.65.

ICP-MS elemental analysis of **Co_{2.05}Ni_{1.95}O₄-dpk** (C₄₈H₄₆Cl₂Co_xNi_{4-x}N₈O₂₂): calc. (%) Co + Ni, 16.9; found (%) Co, 8.16; Ni, 8.58.

ICP-MS elemental analysis of **Co_{1.15}Ni_{2.85}O₄-dpk** (C₄₈H₄₆Cl₂Co_xNi_{4-x}N₈O₂₂): calc. (%) Co + Ni, 16.9; found (%) Co, 4.78; Ni, 11.9.

ICP-MS elemental analysis of **Ni₄O₄-dpk** (C₄₈H₄₆Cl₂Ni₄N₈O₂₂): calc. (%) Ni, 16.9; found (%) Ni, 16.6.

Photocatalytic water oxidation

The deaerated reaction solutions were prepared in a 10 mL glass vial as follows: 9.5 mg Na₂S₂O₈ (5 mM) was added to 8 mL of a buffered solution (pH 7.0 phosphate buffer (80 mM), pH 8.0 borate buffer (80 mM), pH 8.5 borate buffer (40-120 mM), and pH 9.0 borate buffer (80 mM)) containing completely dissolved 6 mg [Ru(bpy)₃]Cl₂·6H₂O (1 mM) and catalyst (desired concentration). Glass vials with the above solutions were sealed with a combination of a rubber septum (PTFE) and an aluminum crimp cap, followed by deaeration through purging with helium (purity 6.0) for 12 min.

O₂ evolution of the above catalytic solutions was measured independently by Clark electrode techniques and gas chromatography. For Clark electrode measurements, an Oxygen sensor (OX-N) Clark electrode (Unisense) was inserted into the deaerated solution through the rubber septum, followed by irradiation with a 470 nm high flux LED light (26.1 mW/cm², Rhopoint Components LTD) after a constant signal of the Clark electrode was obtained under a stirring rate of 1000 rpm. O₂ evolution was monitored with the SensorTrace software (Unisense) applying a frequency of 1 data point per sec. The calibration of the Clark electrode was done according to the procedure provided by the Unisense user manual with a sodium ascorbate solution (2 g sodium ascorbate in 100 mL 0.1 M NaOH solution) as the zero calibration solution and aerated water as the aerated calibration solution (for details cf. Unisense user manual).

For GC measurements, the deaerated solution was irradiated with the above LED light source for 30 min under a stirring rate of 1000 rpm, and a 200 µL gas sample was taken with a gas-tight micro-liter syringe (Hamilton-1825RN) and transferred to the GC injection port. After pushing the syringe bar to the 100 µL mark, 100 µL of the gas sample was quickly injected into the GC (Agilent Technologies 7820A) equipped with a thermal conductivity detector (Varian). O₂ and N₂ were separated by passing the sample through a 3 m * 2 mm packed 5 Å molecular sieve 13X 80-100 column with a helium carrier gas (purity 6.0). Quantification of O₂ evolution was carried out with a good linear GC calibration curve obtained from measuring a series of volumes (50-500 µL) of pure O₂ vs. the peak area of each O₂ signal. Contamination of air was corrected by subtracting the half peak area of N₂ from the peak area of O₂ (due to the similar GC response to O₂ and N₂, the peak area of the contaminating O₂ basically equals 1/3 of the N₂ peak area). The pH value of the post-catalytic solution was measured with a METTLER TOLEDO SevenCompact pH meter.

Recycling tests

Standard activity tests were completed according to the above procedure for photocatalytic water oxidation, and the pH value was readjusted to 8.5 by adding solid Na₂B₄O₇·10H₂O. After adding 9.5 mg of Na₂S₂O₈, the first activity recycling test was started applying the standard procedure. The above procedure was also repeated for the third activity recycling run. O₂ evolution during each test was monitored with a Clark electrode.

¹⁸O isotope-labeling experiments

¹⁸O labeled-photocatalytic water oxidation reactions were carried out according to the above standard procedure using ¹⁸O-enriched water (¹⁸O atom% = 10.8% and 8.3%) instead of normal water. A 100 μ L gas sample from the headspace was injected into a Thermo Scientific Focus GC (run with helium as carrier gas and equipped with a PLTT-5A molsieve 5 PLOT column (30 m * 0.53 mm * 25 μ m)) interfaced with a PolarisQ mass spectrometer (electron impact ionization model) for analysis. The MS detector was tuned for maximum sensitivity, and the single ion mode was selected to scan for the ions of m/z = 28, 32, 34, 36 with a dwell time of 100 ms. The single ion extracted chromatograms were recorded and evaluated for the m/z = 32/34/36 ratios.

pH-dependent UV/vis titration

300 μ M **Co₄O₄-dpk** aqueous solution (4 mL) was titrated by adding sequential aliquots of 0.5 mM NaOH (aq.), and the pH value together with UV/vis spectrum were recorded for each titration, respectively. A titration curve was constructed corresponding to the maximum absorption vs. pH value at this absorption, and the pK_a value was determined as the pH value at the midpoint of the titration curve rise.

Cyclic voltammetry (CV)

CV measurements were carried out on a Metrohm PalmSens3 instrument with glassy carbon, Ag/AgCl (sat. KCl, 0.197 V vs. NHE) and Pt Rod electrodes as working, reference, and auxiliary electrodes. The solutions were deaerated by purging with Ar for 10 min before the measurements. After each measurement, the glassy carbon electrode was polished with alumina slurry, and rinsed with water, 0.1 M HCl, CH₃OH, and CH₂Cl₂. Cyclic voltammograms were recorded in different pH media to obtain the corresponding redox waves of the cobalt centers.

Acetate ligand exchange study

Sequential aliquots of D₂O were added stepwise to a 4.5 mL, 40 mM **Co₄O₄-dpk** (251 mg) CD₃CN solution to obtain 1%, 2%, 4%, 6%, and 8% v/v D₂O containing mixtures, and the FT-IR spectrum was measured for each step on a ReactIR iC 10 FT-IR spectrometer equipped with a Silver Halide (AgX) DSub AgX FiberConduit probe (METTLER TOLEDO). The FT-IR spectrum of HAc-d₄ was recorded from its CD₃CN solution (4.5 mL, 80 mM). The background was obtained from 4.5 mL pure CD₃CN and subtracted from the **Co₄O₄-dpk** and HAc-d₄ measurements.

Buffer ligation study of the {Co₂O₂(OH₂)₂} edge site

For ligation studies in borate buffer, FT-IR spectra of a 6 mL, 40 mM **Co₄O₄-dpk** (251 mg) CH₃CN solution were recorded before and after adding 1 mL of 240 mM borate buffer aqueous solution, respectively. The backgrounds were obtained from 6 mL pure CH₃CN and 6 mL CH₃CN + 1 mL borate buffer aqueous solution (240 mM), respectively, and subtracted from the **Co₄O₄-dpk** measurements. The same procedure was applied for the phosphate buffer study by using formamide and Na₂HPO₄ instead of CH₃CN and borate buffer.

X-ray absorption spectroscopy

Experiments have been performed at the SuperXAS beamline of the Swiss Light Source (SLS), Villigen, Switzerland. The storage ring was run in the top-up mode with an average current of 400 mA. The X-ray beam was collimated by a Si coated mirror and the energy was scanned by a channel-cut Si(111) monochromator. Energy calibration was performed using metal Co foil (with the maximum of the first derivative of the spectrum at 7709 eV). A toroidal mirror with Rh coating was employed after the monochromator to focus the incident X-rays with a spot size of 140×120 μ m² on the sample. The photon flux at the sample was measured to be 3.3×10¹¹ photons/s. Measurements were performed in the fluorescence mode using 5-element Silicon Drift Detector (SDD). Z-1 filter (Fe foil) with absorption edge jump 4.5 was placed at 9 mm distance from the detector and an additional collimator was placed between filter and sensors of the detector to reduce the re-fluorescence from the filter that reaches the detector and to minimize the background from the elastic scattering of the incident beam. For in-situ experiments the sample was circulated in the flow system with the X-ray beam interacting with the open cylindrical jet of the sample (1 mm diameter). The total volume of sample in the flow system was ~50 mL. The use of the flow system with rather large volume allowed to avoid any observable X-ray-induced damage of the sample, which was confirmed by a large series of short scans (a few minutes each) for initial state of the catalyst. Sample container was irradiated with high-power collimated LED source (Mightex, model LCS-0405-12-48) with 405 nm wavelength, 48 mm aperture, and the output power up to 975 mW.

In situ photochemistry: The sample (100 μ M **Co₄O₄-dpk**, 1 mM PS, 5 mM Na₂S₂O₈, in 50 mL borate buffer pH 8.5) was cycled in the open jet in order to prevent the accumulation of radiation damage.

Freeze quench experiments: XAFS data were recorded at 40 K using the He-cryostat. The samples were prepared as follows: 1 mL of 0.5 mM **Co₄O₄-dpk** (in pH 8.5, 80 mM borate buffer) was mixed with 1 mL of a [Ru(bpy)₃](ClO₄)₃ solution (0.5 – 20 mM, miliQ). After 1 min mixing time, 0.1 mL of the solution were rapidly frozen on the pre-cooled cooper sample holder (~77 K). The sample was transferred quickly into the cryostat.

Data treatment: Energy calibration, background removal, Fourier transformation, and linear compination fit of XAS spectra were performed with the Athena software, and EXAFS fits were performed with the Artemis software.¹

Chemical oxidation of Co₄O₄-dpk

Clark electrode kinetics: 4 mL of 0.5 mM **Co₄O₄-dpk** solution (pH 8.5, 80 mM borate buffer) was mixed with 4 mL [Ru(bpy)₃](ClO₄)₃ solution (2.5 – 19.25 mM, milliQ). Oxygen evolution was recorded with a Clark electrode applying the same settings in the photocatalytic experiments.

UV/vis kinetics: 1 mL of 0.5 mM **Co₄O₄-dpk** solution (pH 8.5, 80 mM borate buffer) was mixed with 1 mL [Ru(bpy)₃](ClO₄)₃ solution (2.5 – 19.25 mM, milliQ). Single wavelength absorption data at the absorption maximum of [Ru(bpy)₃](ClO₄)₃ (675 nm) were recorded applying a frequency of 1 data point per sec.

Crystallographic information and structural description of Co₄O₄-dpk

A suitable single crystal was selected, mounted on a glass fiber loop with Infineum oil, and placed in a cooled N₂ gas stream at 183 K. X-ray diffraction intensity data collection was performed on an Oxford Xcalibur Ruby CCD diffractometer equipped with an enhanced Mo X-ray source (Mo K α , λ = 0.71073 Å) and a graphite monochromator. All data processing and an absorption correction (multi-scan) were carried out using the program CrysAlisPro (1.171.37.35. Agilent (2014)). Structure solution and refinement were performed using the Olex2 1.2 software package.² An initial structure solution was obtained from SHELXT (2014/4),³ and refined with SHELXL (2014/7).⁴ Crystal data, data collection parameters, and refinement statistics are listed in **Table S1**. An ORTEP representation of **Co₄O₄-dpk** is displayed in **Figure S1**.

The crystal structure of **Co₄O₄-dpk** is constituted of the tetranuclear Co-containing cation [Co₄(dpy{OH}O)₄(OAc)₂(H₂O)₂]²⁺ and two well-separated ClO₄⁻ counteranions. ClO₄⁻ exhibits disorder with the occupancies of 0.69 and 0.31 for Cl1, O8 and Cl2, O12, respectively, and it is located close to the aqua ligand. A hydrogen bond is formed between O9 of ClO₄⁻ and H5a of the neighboring aqua ligand. The [Co₄(dpy{OH}O)₄(OAc)₂(H₂O)₂]²⁺ cation and two ClO₄⁻ anions are located on the same two-fold axis. The four Co atoms of the {Co₄O₄} cubic core are connected by 4 O atoms from 4 dpd-H ligands. The Co centers can be classified into two different types, namely Co1/Co1a and Co2/Co2a, in line with the molecular symmetry of **Co₄O₄-dpk**. Co1 is coordinated by a single N atom from one of the dpd-H ligands and by 2 O atoms from different dpd-H ligands. Additionally, one H₂O and one monodentate acetate ligand are also coordinated to Co1 vertically and horizontally to the {Co1OCo1aO} plane, respectively. Co2 is exclusively coordinated by 3 N atoms and 3 O atoms from different (dpy{OH}O) ligands.

(1) Ravel, B.; Newville, M. *J. Synchrotron Rad.* **2005**, *12*, 537–541.

(2) Dolomanov, O. V.; Bourhis, L. J.; Gildea, R. J.; Howard, J. A. K.; Puschmann, H. *J. Appl. Cryst.* **2009**, *42*, 339–341.

(3) Sheldrick, G. M. *Acta Cryst.* **2015**, *A71*, 3–8.

(4) Sheldrick, G. M. *Acta Cryst.* **2015**, *C71*, 3–8.

Table S1. Crystallographic and structural refinement data of [Co₄(dpy{OH}O)₄(OAc)₂(H₂O)₂](ClO₄)₂.

Empirical formula	C ₄₈ H ₄₆ Cl ₂ Co ₄ N ₈ O ₂₂
Formula weight	1393.55 g·mol ⁻¹
Temperature	183 K
Radiation wavelength	0.71073 Å
Crystal system	monoclinic
Space group	C2/c
<i>a</i>	22.8068(9) Å
<i>b</i>	12.1904(4) Å
<i>c</i>	21.0805(7) Å
α	90°
β	115.750(5)°
γ	90°
Volume	5278.9(4) Å ³
<i>Z</i>	4
Density calcd.	1.753 g·cm ⁻³
Absorption coefficient	1.428 mm ⁻¹ (analytical)
Crystal size (mm)	0.322 × 0.195 × 0.104
Independent reflections	5396 [R _{int} = 0.0449]
Reflections collected	54440
θ range	2.418–26.371°
Completeness to $\theta = 26.32^\circ$	0.999
F(000)	2832
Data/restraints/parameters	5396/79/402
$R_1[I > 2\sigma(I)]^a$	0.0598
$wR_2[I > 2\sigma(I)]^b$	0.1495
R_1^a (all data)	0.0712
wR_2^b (all data)	0.1589
Goodness-of-fit on F ²	1.050

$$^a R_1 = \sum ||F_o| - |F_c|| / \sum |F_o|; ^b wR_2 = \{ \sum [w(F_o^2 - F_c^2)^2] / \sum [w(F_o^2)^2] \}^{1/2}$$

Table S2. Selected bond lengths and distances of Co₄O₄-dpk.

Bond	d (Å)	Bond	d (Å)
Co1-Co1a	3.165	Co2-Co2a	3.072
Co1-Co2a Co1a-Co2	3.299	Co1-Co2 Co1a-Co2a	3.207
Co1-O1 Co1a-O1a	2.067(3)	Co2-O1 Co2a-O1a	2.151(3)
Co1-O1a Co1a-O1	2.138(3)	Co2-O3 Co2a-O3a	2.050(3)
Co1-O3a Co1a-O3	2.176(3)	Co2-O3a Co2a-O3	2.116(3)
Co1-O5 Co1a-O5a	2.105(4)	Co2-N2 Co2a-N2a	2.071(4)
Co1-O6 Co1a-O6a	2.027(3)	Co2-N3 Co2a-N3a	2.131(3)
Co1-N1 Co1a-N1a	2.129(4)	Co2-N4a Co2a-N4	2.134(4)

Table S3. Bond valence sum (BVS) calculations for the Co centers of **Co₄O₄-dpk**.

Atom	BVS	Atom	BVS
Co1/Co1a	1.97	Co2/Co2a	1.95

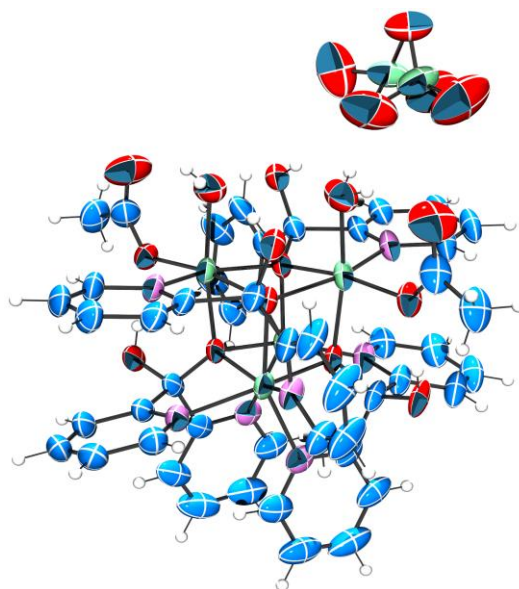


Figure S1a. ORTEP representation of **Co₄O₄-dpk** (50% probability level).

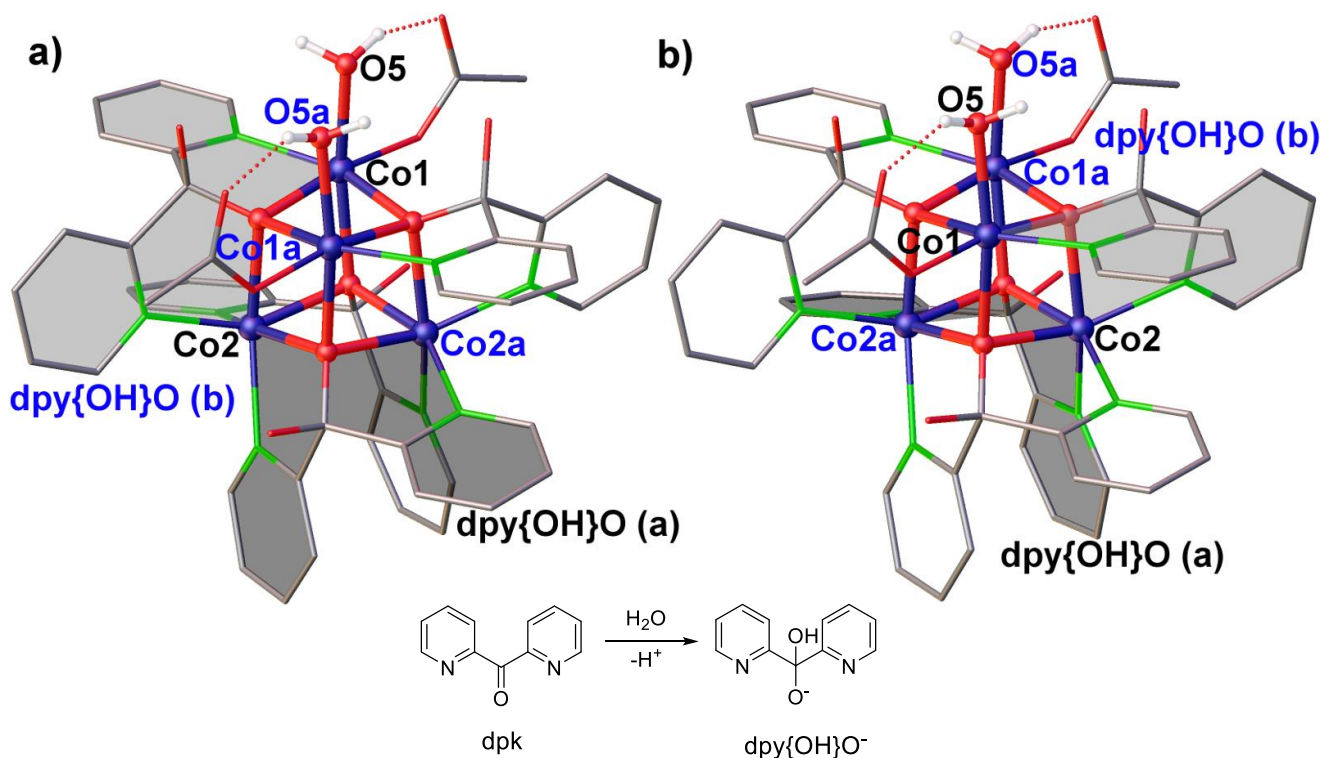


Figure S1b. Top: Crystal structure of **Co₄O₄-dpk** with the crystallographically different dpy{OH}O ligands highlighted; Co: dark blue, C: grey, O: red, N: green, H: white; **a** and **b** are related through a C_2 operation; bottom: formation of the dpy{OH}O⁻ ligand.

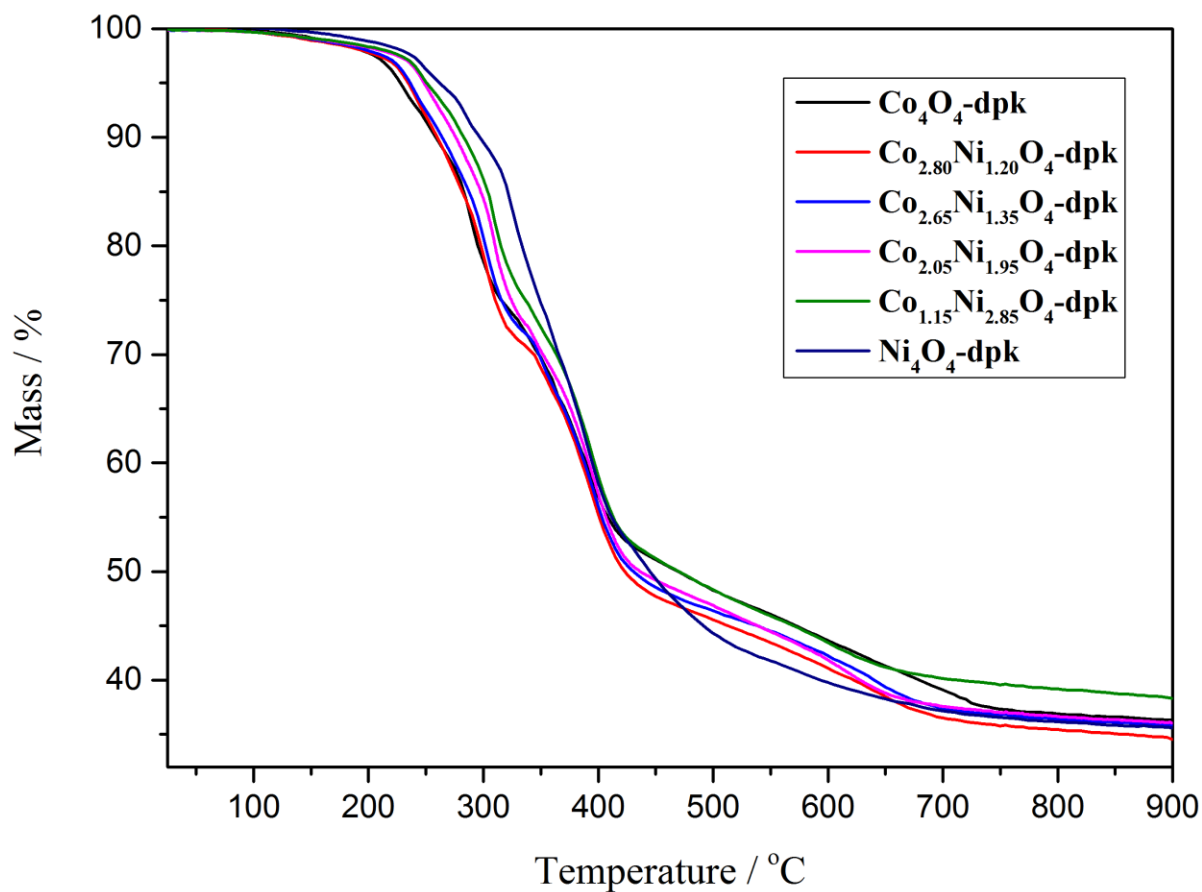


Figure S2. Thermogravimetric characterization of $\text{Co}_4\text{O}_4\text{-dpk}$, the $\text{Co}_x\text{Ni}_{4-x}\text{O}_4\text{-dpk}$ series, and $\text{Ni}_4\text{O}_4\text{-dpk}$.

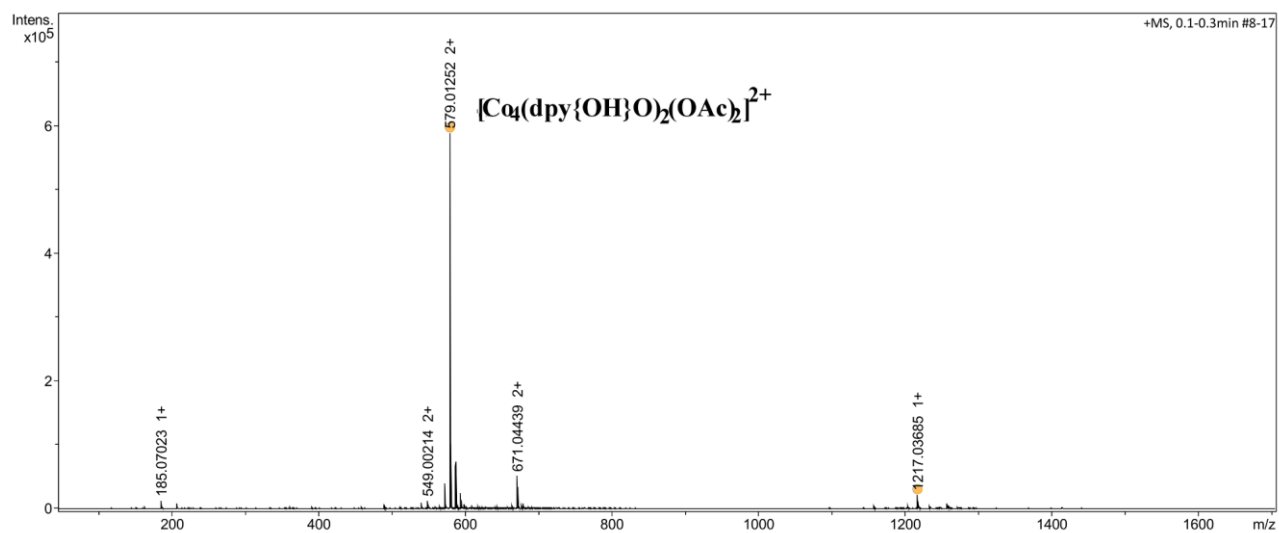


Figure S3. HR-ESI-MS spectrum of $\text{Co}_4\text{O}_4\text{-dpk}$.

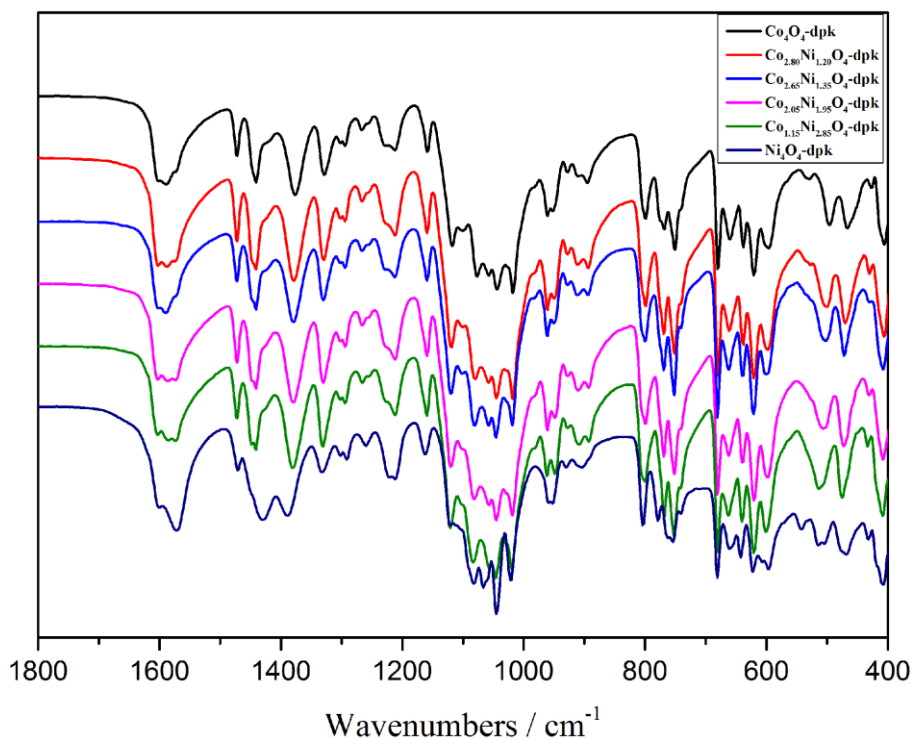


Figure S4. FT-IR spectra of **Co₄O₄-dpk**, **Ni₄O₄-dpk**, and the **Co_xNi_{4-x}O₄-dpk** series.

1603 cm⁻¹ (m): single C-O stretching vibration of the (dpy{OH}O) ligand;
 1472 (m), 1442 (m), and 1379 (m) cm⁻¹: stretching vibrations of the 2-pyridyl rings; 1571 cm⁻¹ (m, overlapping with 1603 cm⁻¹): asymmetrical vibrations of COO⁻; 1329 cm⁻¹ (m): symmetric vibrations of COO⁻; 620 cm⁻¹ (s): $\nu_4(\text{F}_2)$ of the uncoordinated T_d ClO₄⁻; 682 cm⁻¹ (s), 801 (m), 770 (s), and 755 (s) cm⁻¹: C-H out-of-plane vibrations of the 2-pyridyl rings; C-H in-plane vibrations of the 2-pyridyl rings.

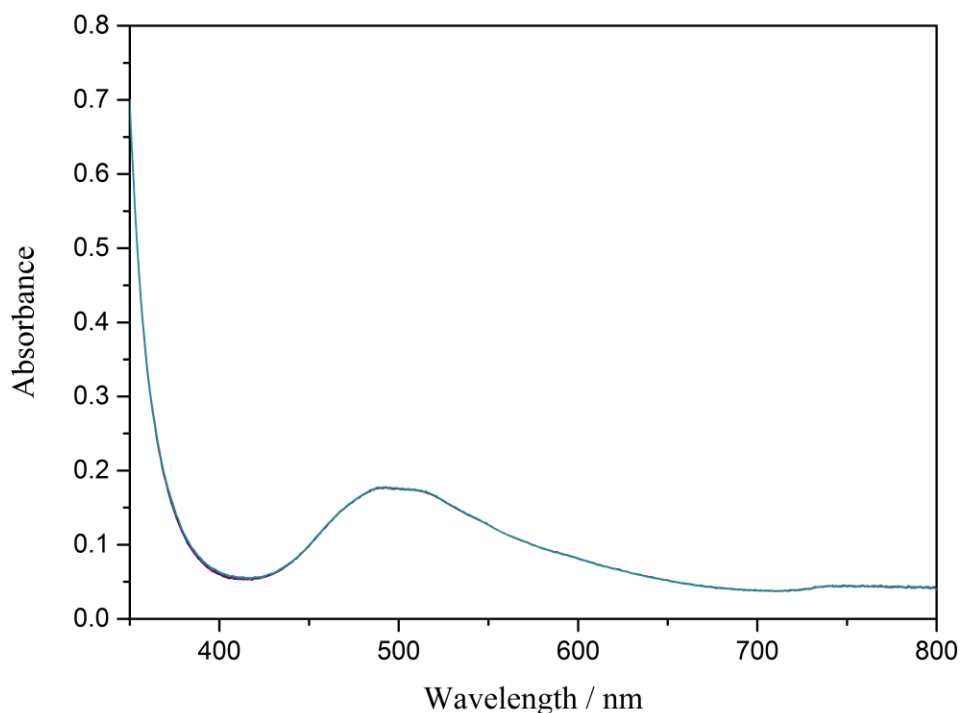


Figure S5. Time dependent UV/vis spectra of 1.5 mM **Co₄O₄-dpk** in pH 8.5, 80 mM borate buffer solution over 2 h.

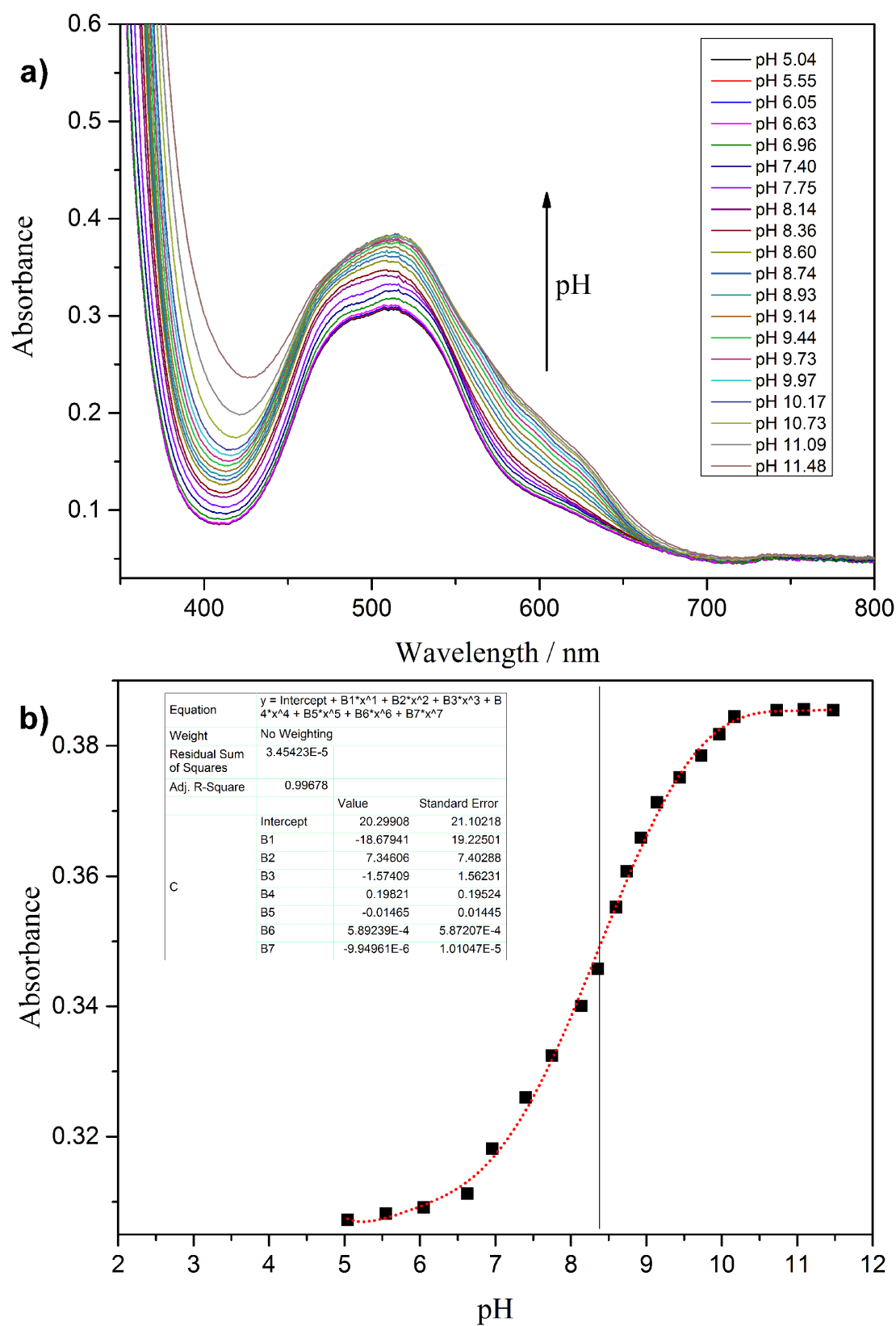


Figure S6. (a) pH dependent UV/vis spectra of 3 mM **Co₄O₄-dpk** cubane; (b) representative plot of the absorbance at 516 nm vs. pH.

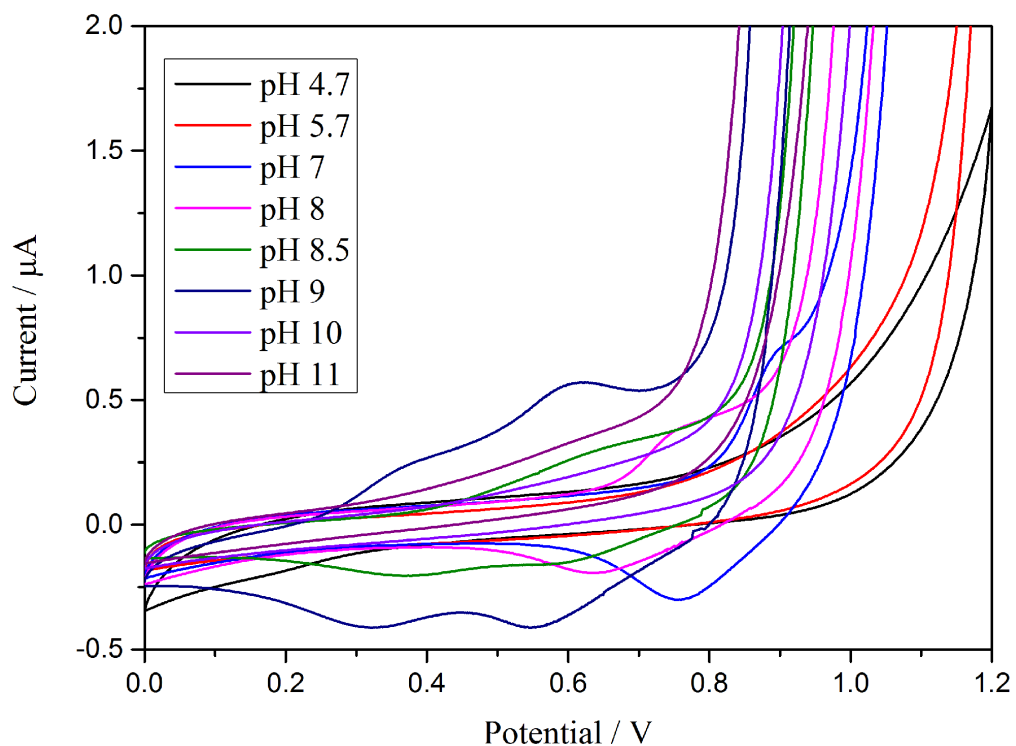


Figure S7. Cyclic voltammograms of 1 mM $\text{Co}_4\text{O}_4\text{-dpk}$ in the pH range of 4.7-11.

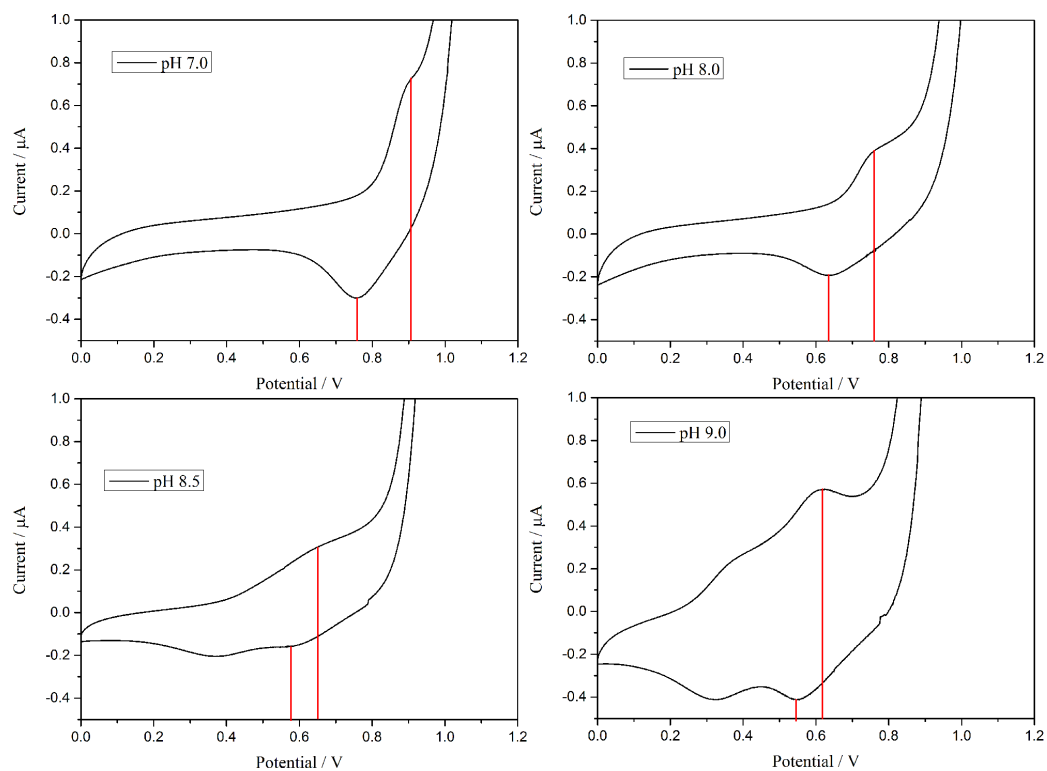


Figure S8. Cyclic voltammograms of 1 mM $\text{Co}_4\text{O}_4\text{-dpk}$ in the pH range of 7.0-9.0.

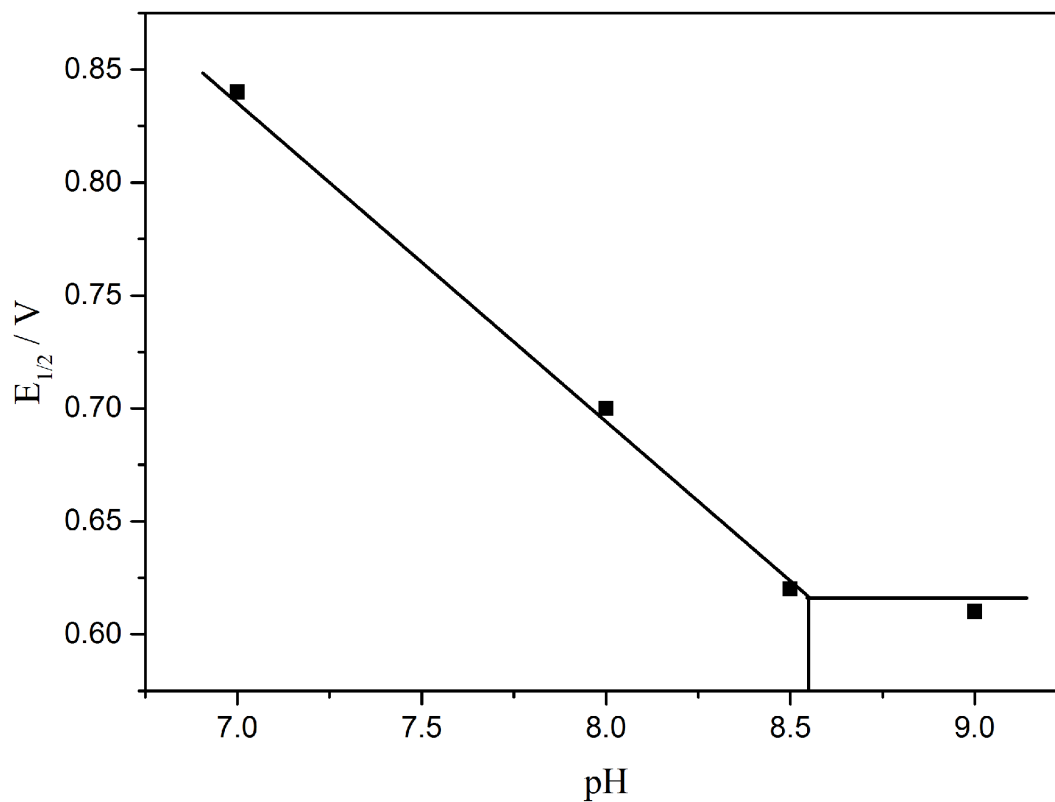


Figure S9. Pourbaix diagram of 1 mM $\text{Co}_4\text{O}_4\text{-dpk}$ in the pH range of 7-9.

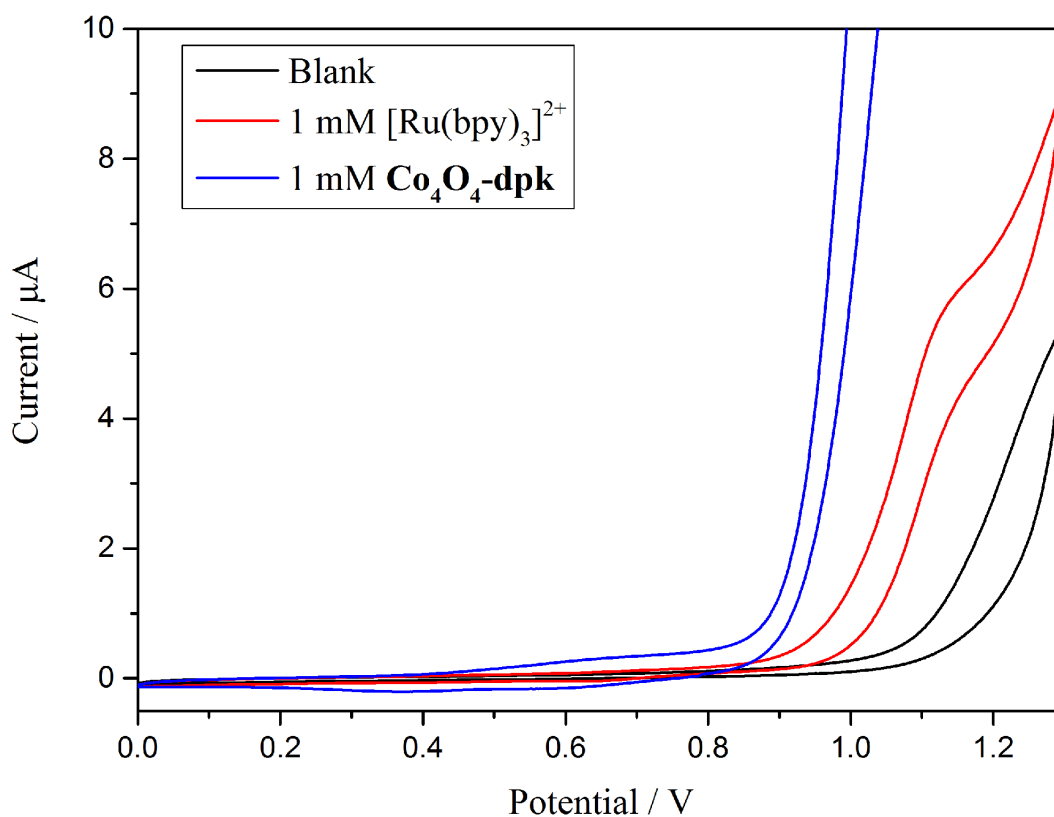


Figure S10. Cyclic voltammograms of 1 mM $\text{Co}_4\text{O}_4\text{-dpk}$ (blue) and 1 mM $[\text{Ru}(\text{bpy})_3]\text{Cl}_2$ (red) in 80 mM pH 8.5 borate buffer.

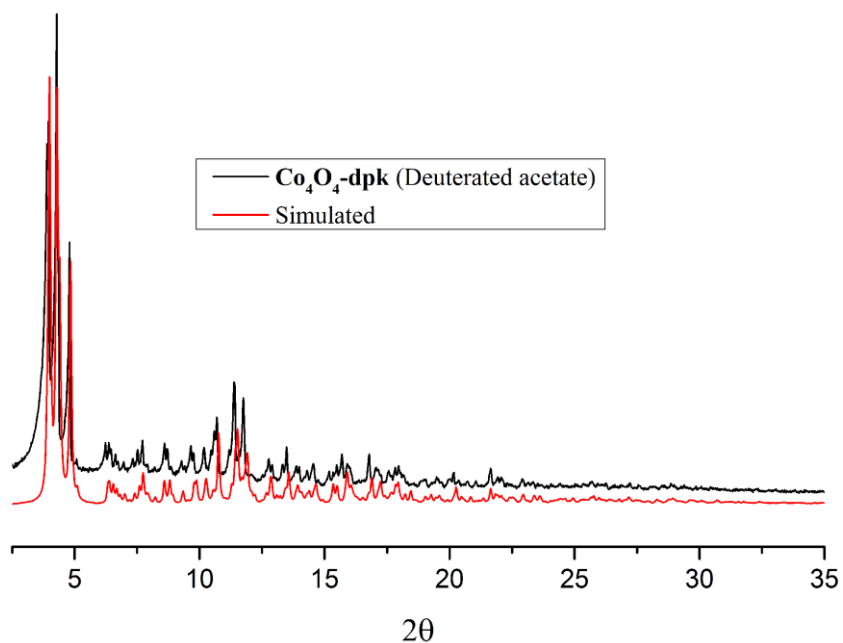


Figure S11. PXRD pattern (black) of **Co₄O₄-dpk(OAc-d₃)** vs. calculated data (red).

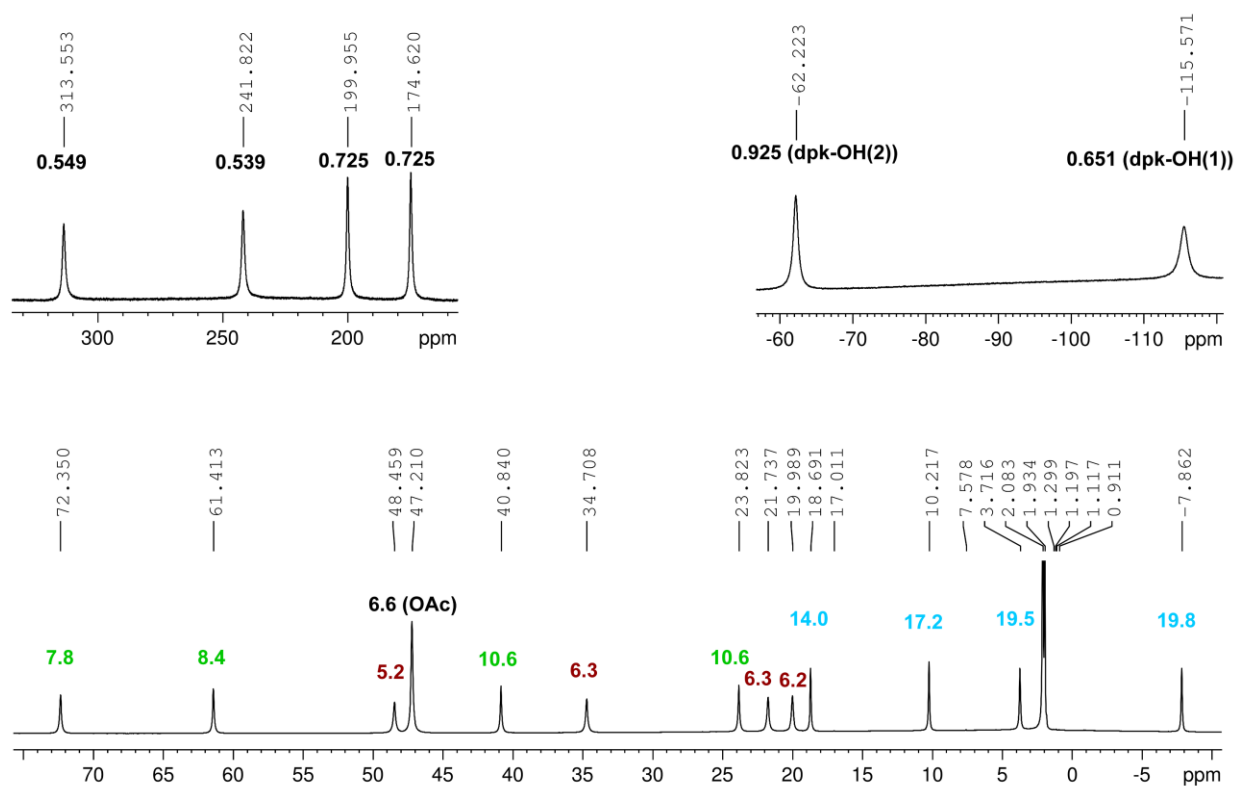


Figure S12. ¹H NMR spectrum of **Co₄O₄-dpk** in CD₃CN with T₁ values given in ms (proton groups are indicated by the following color code (cf. Figure 3): black = ortho, red = meta(1), green = meta(2), blue = para).

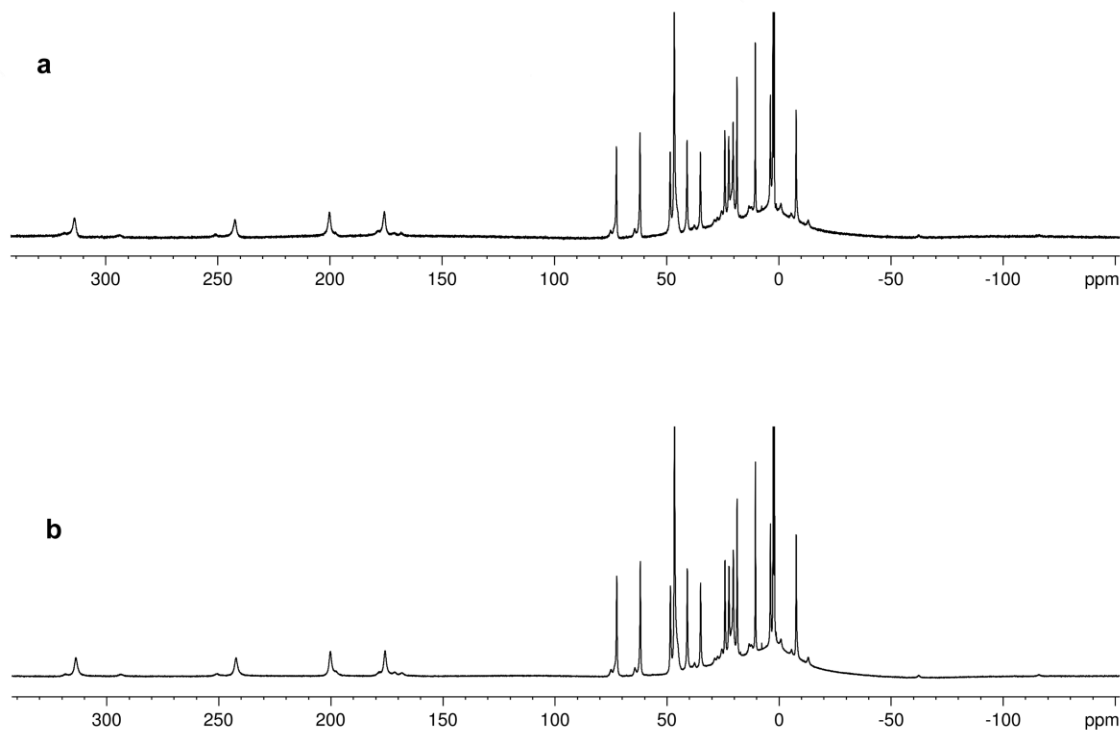


Figure S13. ^1H NMR spectrum of **Co₄O₄-dpk** in CD_3CN (a) immediately after D_2O addition and (b) 30 h later.

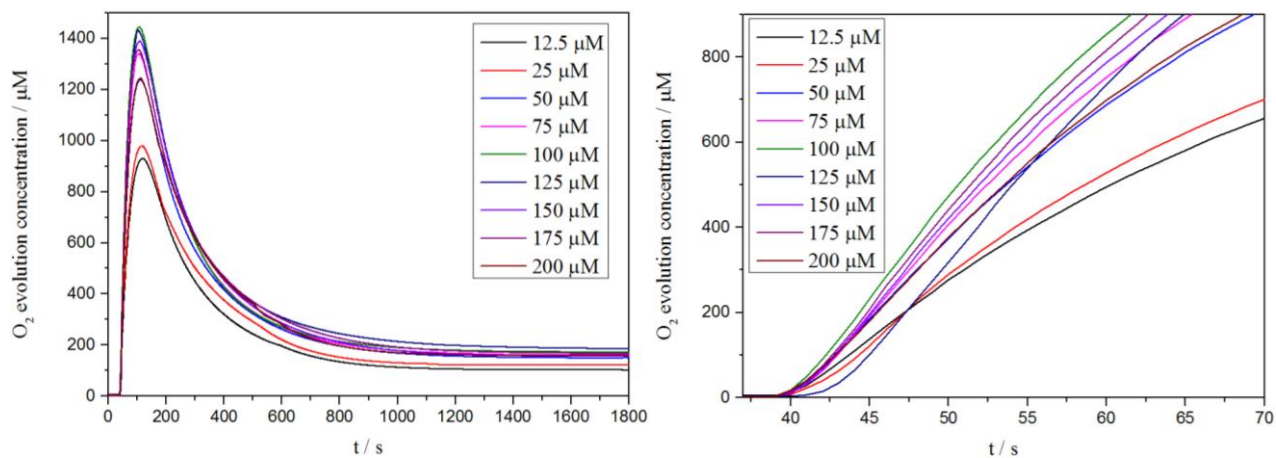


Figure S14. Clark electrode kinetics of visible light-driven water oxidation catalyzed by various concentrations of **Co₄O₄-dpk** cubane (conditions: 470 nm LED; 1 mM $[\text{Ru}(\text{bpy})_3]\text{Cl}_2$; 5 mM $\text{Na}_2\text{S}_2\text{O}_8$; pH 8.5, 80 mM borate buffer).

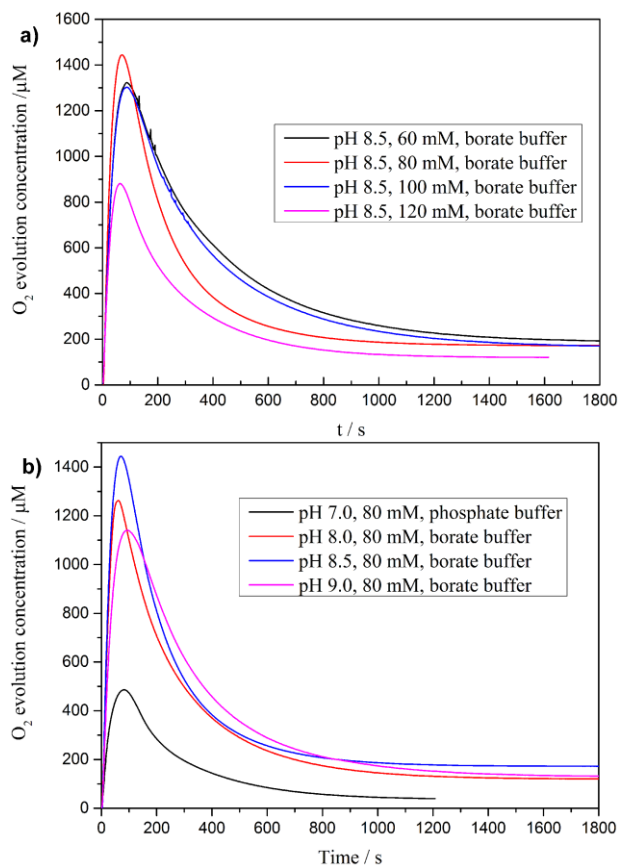


Figure S15. (a) Clark electrode kinetics (long-time data of Figure 4) of visible light-driven water oxidation catalyzed by **Co₄O₄-dpk** cubane in different concentrations of pH 8.5 borate buffer; (b) visible light-driven water oxidation catalyzed by 100 μM of **Co₄O₄-dpk** at pH 7.0 (80 mM phosphate buffer solution), 8.0, 8.5, and 9.0 (80 mM borate buffer solution, respectively); conditions: 470 nm LED; 1 mM [Ru(bpy)₃]Cl₂; 5 mM Na₂S₂O₈.

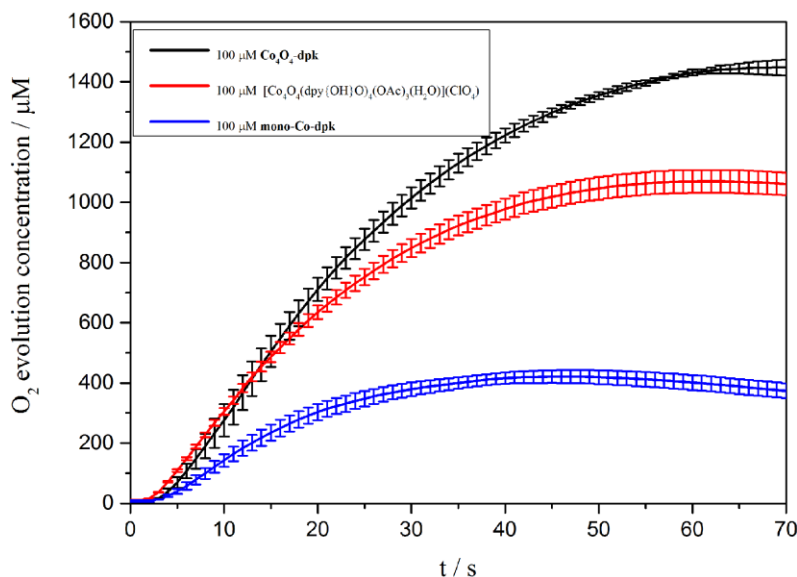


Figure S16. Clark electrode kinetics of visible light-driven water oxidation catalyzed by 100 μM of **Co₄O₄-dpk** (black), **[Co₄O₄(dpy{OH}O)₄(OAc)₃(H₂O)](ClO₄)** (red), and **[Co^{III}(dpy{OH}O)₂](ClO₄)** (**mono-Co-dpk**), respectively (blue); conditions: 470 nm LED; 1 mM [Ru(bpy)₃]Cl₂; 5 mM Na₂S₂O₈; pH 8.5, 80 mM borate buffer.

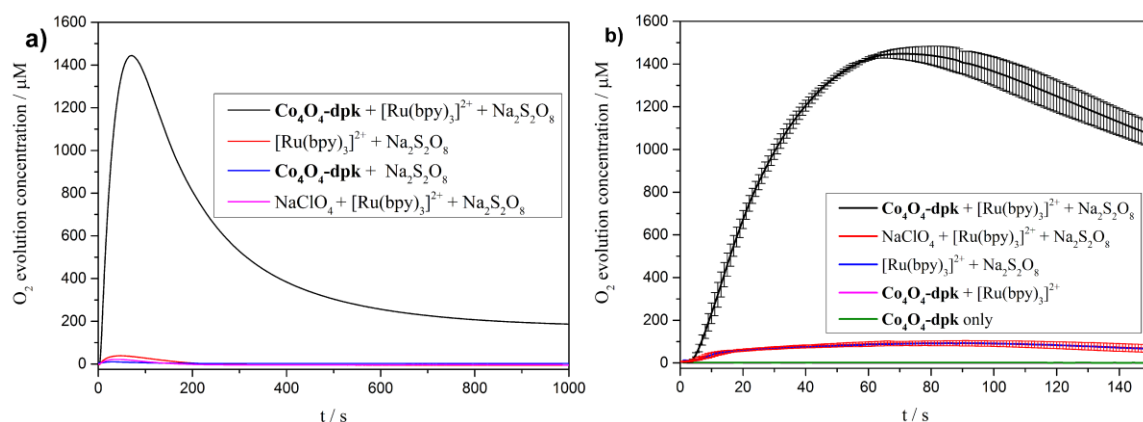


Figure S17. (a) Clark electrode kinetics of visible light-driven water oxidation catalyzed by 100 μM of **Co₄O₄-dpk** (black), 200 μM NaClO₄ (pink) vs. no catalyst (red) and of a control experiment without [Ru(bpy)₃]Cl₂ (blue), respectively; (b) additional control experiments in the presence of 100 μM of **Co₄O₄-dpk** and [Ru(bpy)₃]Cl₂ (pink) and of **Co₄O₄-dpk** only (green) (conditions: 470 nm LED; 1 mM [Ru(bpy)₃]Cl₂; 5 mM Na₂S₂O₈; pH 8.5, 80 mM borate buffer).

Table S4. Photocatalytic water oxidation performance with different concentrations of **Co₄O₄-dpk**.

Catalyst concentration/μM	O ₂ area	N ₂ area	O ₂ /μmol	^a O ₂ yield	^b TON	^c TOF / s ⁻¹
12.5	892.7	34.5	9.6	48%	96.0	1.2
25	1075.4	55.8	11.5	57.5%	57.5	0.63
50	1215.3	56.5	13.1	65.5%	32.8	0.40
75	1341.8	33.8	14.4	72.0%	24.0	0.30
100	1488.8	55.4	16.0	80.0%	20.0	0.24
125	1377.3	48.3	14.8	74.0%	14.8	0.19
150	1388	77	14.7	73.5%	12.2	0.15
175	1338.3	17.2	14.5	72.5%	10.4	0.13
200	1314	24.3	14.2	71.1%	8.88	0.10

^aO₂ yield = 2 × mole of O₂ (GC)/mole of Na₂S₂O₈. ^bTON = mole of O₂ (GC)/mole of catalyst. ^cTOF_{initial} = initial concentration of O₂ evolution rate (Clark electrode kinetics in 60 s)/catalyst concentration. Conditions: 470 nm LED; pH 8.5 80 mM, borate buffer; 1 mM [Ru(bpy)₃]Cl₂; 5 mM Na₂S₂O₈.

Table S5. Photocatalytic water oxidation performance of **Co₄O₄-dpk** in different buffer solutions.

Buffer solution /type	O ₂ area	N ₂ area	O ₂ /μmol	^a O ₂ yield	^b TON	^c TOF / s ⁻¹
pH 7.0 80 mM phosphate	204.2	21.2	2.4	12%	3.0	0.08
pH 8.0 80 mM phosphate	621.3	63.1	6.7	34%	8.4	
pH 8.0 80 mM borate buffer	1020.5	34.9	11.0	55.0%	13.8	0.18
pH 8.5 80 mM borate buffer	1488.8	55.4	16.0	80%	20.0	0.24
pH 9.0 80 mM borate buffer	1247.8	24.5	13.5	67.5%	16.9	0.21

^aO₂ yield = 2 × mole of O₂ (GC)/mole of Na₂S₂O₈. ^bTON = mole of O₂ (GC)/mole of catalyst. ^cTOF_{initial} = initial concentration of O₂ evolution rate (Clark electrode kinetics in 60 s)/catalyst concentration. Conditions: 470 nm LED; 100 μM of **Co₄O₄-dpk**; 1 mM [Ru(bpy)₃]Cl₂; 5 mM Na₂S₂O₈.

Table S6. Photocatalytic water oxidation performance of **Co₄O₄-dpk** in different concentrations of borate buffer.

Borate buffer pH 8.5 concentration	O ₂ area	N ₂ area	O ₂ /μmol	^a O ₂ yield	^b TON	^c TOF / s ⁻¹
40 mM	1072.1	40.2	11.5	57.5%	14.4	
60 mM	1269.5	11.8	13.8	69.0%	17.2	0.21
80 mM	1488.8	55.4	16.0	80%	20.0	0.24
90 mM	1280.5	11	14.0	70%	17.5	0.20
100 mM	1271.4	25.3	13.8	69.0%	17.2	0.20
120 mM	1170.6	21.5	12.7	63.5%	15.9	0.15

^aO₂ yield = 2 × mole of O₂ (GC)/mole of Na₂S₂O₈. ^bTON = mole of O₂ (GC)/mole of catalyst. ^cTOF_{initial} = initial concentration of O₂ evolution rate (Clark electrode kinetics in 60 s)/catalyst concentration. Conditions: 470 nm LED; 100 μM of **Co₄O₄-dpk**; 1 mM [Ru(bpy)₃]Cl₂; 5 mM Na₂S₂O₈.

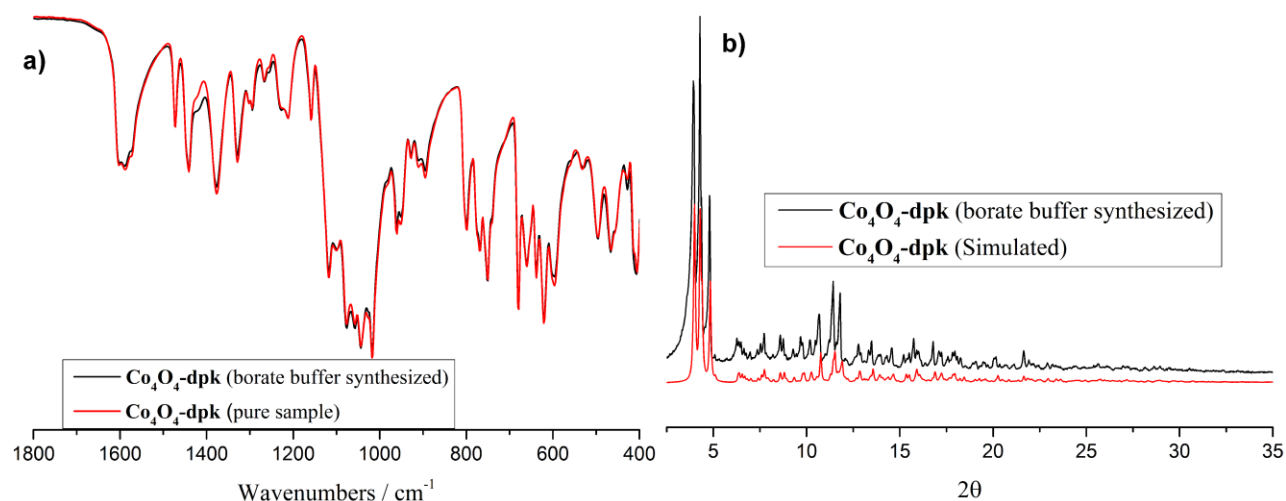


Figure S18. (a) FT-IR spectra of **Co₄O₄-dpk** synthesized from borate buffer (black) vs. pristine **Co₄O₄-dpk** (red), (b) PXRD pattern (black) of **Co₄O₄-dpk** synthesized from borate buffer solution vs. calculated PXRD pattern of **Co₄O₄-dpk** (red).

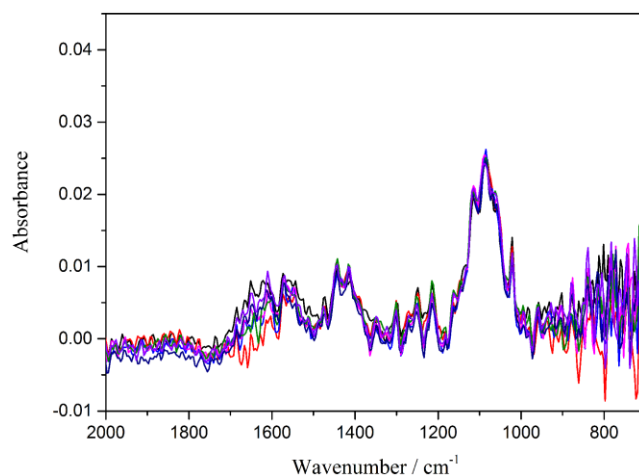


Figure S19. Time-dependent FT-IR spectra of **Co₄O₄-dpk** cubane (20 mM) in pH 8.5, 80 mM borate buffer over 2 h.

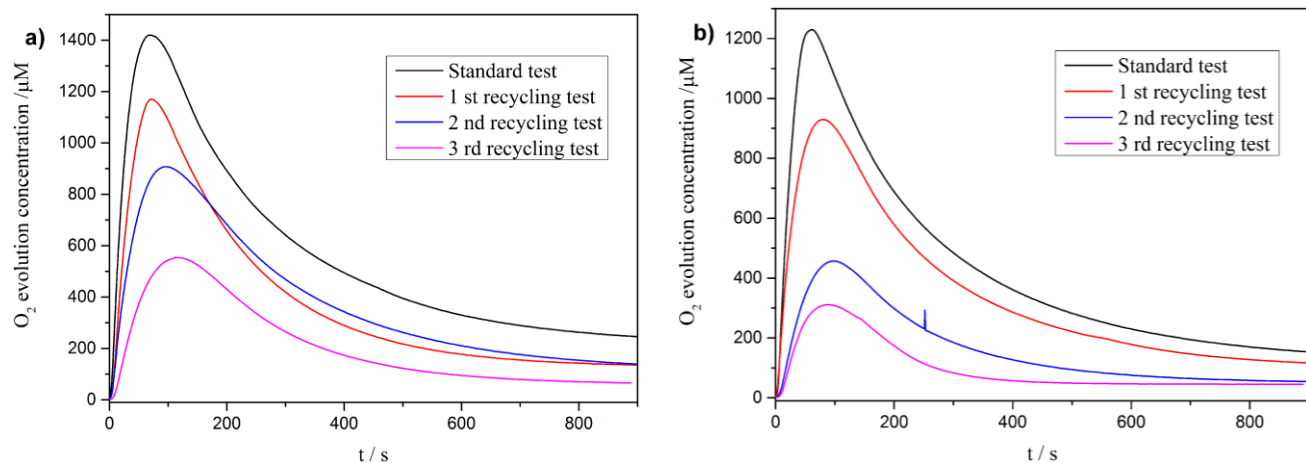


Figure S20. (a) Clark electrode kinetics of visible light-driven water oxidation of the recycling test of 100 μM $\text{Co}_4\text{O}_4\text{-dpk}$ cubane vs. (b) 400 μM $\text{Co}_2(\text{OAc})_2$ (conditions: 470 nm LED; 1 mM $[\text{Ru}(\text{bpy})_3]\text{Cl}_2$; 5 mM $\text{Na}_2\text{S}_2\text{O}_8$; pH 8.5, 80 mM (only the standard test solution) borate buffer), respectively. The pH value was readjusted to 8.5 by adding solid $\text{Na}_2\text{B}_4\text{O}_7$ after each activity test. (Both series were recorded within several hours on the same day based on the same calibration of the applied Clark electrode.)

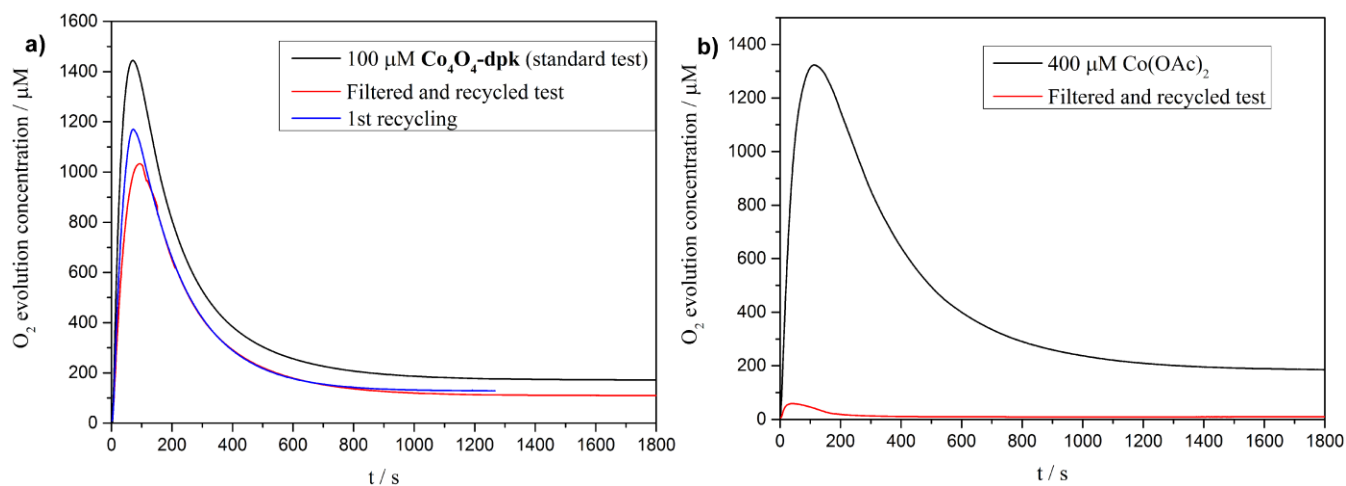


Figure S21. Clark electrode kinetics of visible light-driven water oxidation of the filtered post-catalytic reaction solutions of 100 μM $\text{Co}_4\text{O}_4\text{-dpk}$ cubane (a) and 400 μM $\text{Co}(\text{OAc})_2$ (b) (conditions: 470 nm LED; 1 mM $[\text{Ru}(\text{bpy})_3]\text{Cl}_2$; 5 mM $\text{Na}_2\text{S}_2\text{O}_8$; pH 8.5, 80 mM (only the standard test solution) borate buffer), respectively. The pH value was readjusted to 8.5 by adding solid $\text{Na}_2\text{B}_4\text{O}_7$ after each activity test.

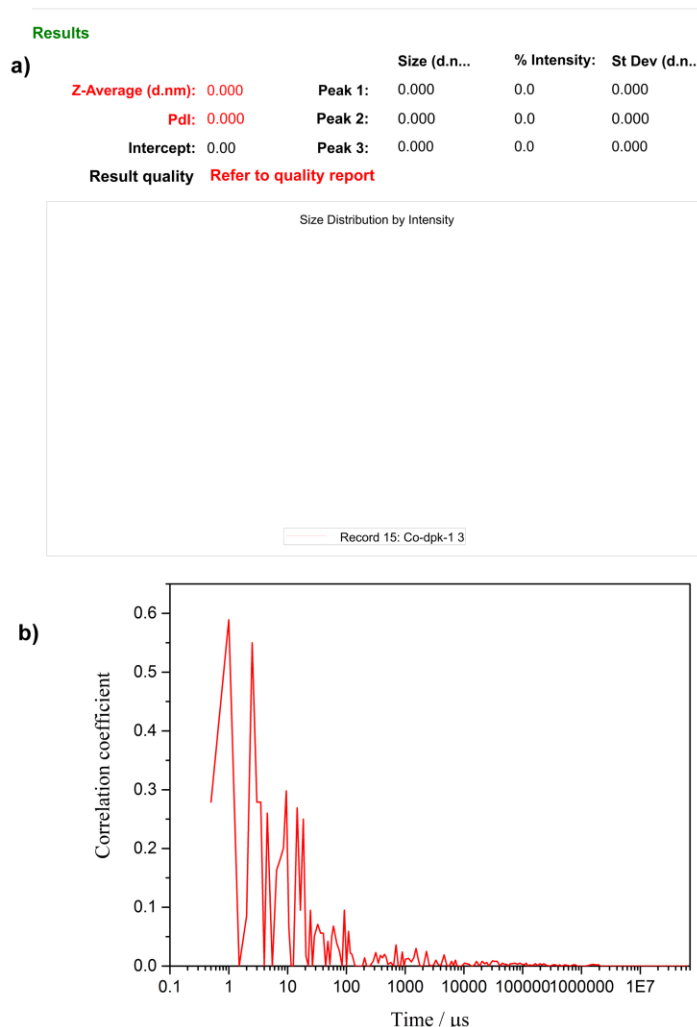


Figure S22. Dynamic light scattering measurement of the post-catalytic reaction solution of 100 μM **Co₄O₄-dpk** cubane (470 nm LED, pH 8.5, 80 mM borate buffer, 1 mM [Ru(bpy)₃]Cl₂, 5 mM Na₂S₂O₈): (a) size distribution report; (b) low quality correlation function with a very small count rate of 3.5 kps indicating the existence of only a very small amount of nanoparticles.

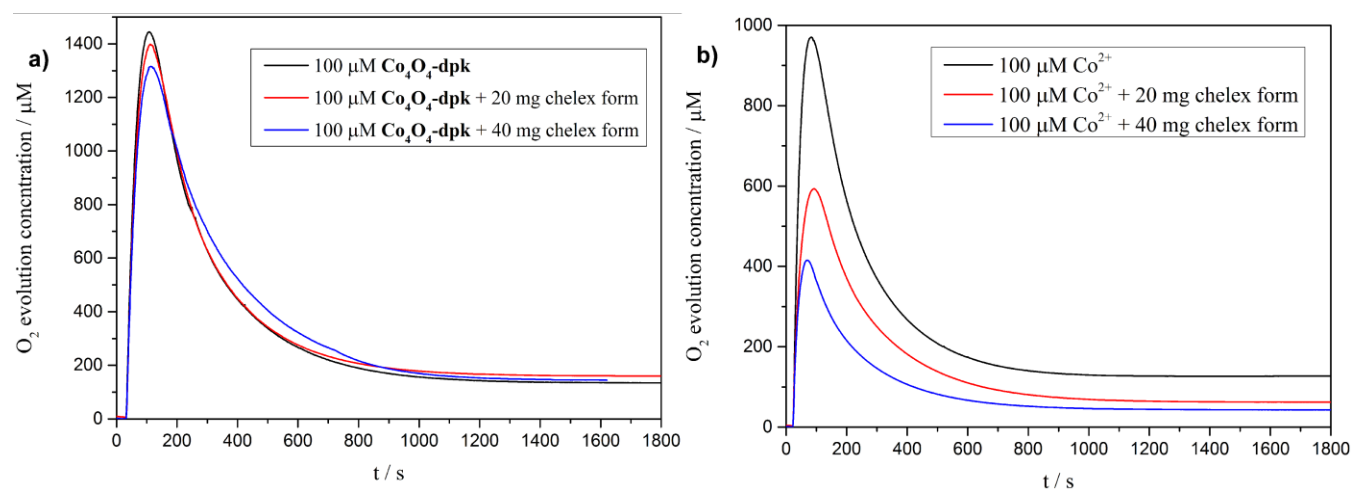


Figure S23. (a) Clark electrode kinetics of visible light-driven water oxidation catalyzed by 100 μM **Co₄O₄-dpk** cubane chelated by different amounts of Chelex (sodium form) vs. (b) 100 μM Co(OAc)₂ (conditions: 470 nm LED; 1 mM [Ru(bpy)₃]Cl₂; 5 mM Na₂S₂O₈; pH 8.5, 80 mM borate buffer).

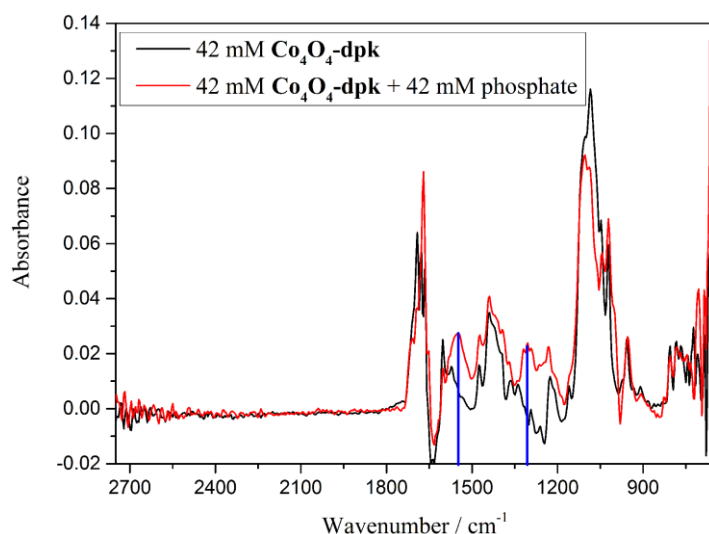


Figure S24. FT-IR spectra of **Co₄O₄-dpk** (42 mM) in pure formamide (black) and in formamide containing 42 mM phosphate (red).

Table S7. Selected distances and Debye-Waller factors from the EXAFS fit for **Co₄O₄-dpk** before and after photocatalytic oxygen evolution.

In the EXAFS fit, we used 8 and 10 fitting parameters for the precatalytic and postcatalytic sample, respectively. Since 12 and 15 parameters could be used for the precatalytic and postcatalytic sample, respectively, according to the Nyquist criterion,¹ both fits can be considered as reasonable. For both EXAFS fits the applied parameters include a parameter for refinement of the amplitude and a parameter for the energy shift E_0 , and these parameters were used as global parameters for all scattering paths. The distances were changed proportionally using 4 and 5 independent parameters for the precatalytic and postcatalytic sample, respectively. The Debye-Waller factors were refined using 2 and 3 independent parameters based on the chemical nature of the scattering atom for the precatalytic and postcatalytic sample, respectively.

		N	pre catalysis		post catalysis		$r_{\text{SXRD}}/\text{\AA}$
			$\sigma^2/10^{-3}\text{\AA}^2$	$r/\text{\AA}$	$\sigma^2/10^{-3}\text{\AA}^2$	$r/\text{\AA}$	
Co1	O3	1	9±5	2.03±0.02	4±1	1.857±0.008	2.050
	N2	1	6±2	2.05±0.02	4±1	1.876±0.009	2.071
	O3	1	9±5	2.09±0.02	4±1	1.97±0.03	2.116
	N3	2	6±2	2.17±0.02	4±1	2.13±0.02	2.133
	O1	1	9±5	2.19±0.02	4±1	2.14±0.02	2.151
	Co1	1	2.3±0.8	3.07±0.01	12±3	2.97±0.03	3.072
	Co2.1	1	2.3±0.8	3.21±0.01	12±3	3.10±0.04	3.207
	Co2.2	1	2.3±0.8	3.30±0.01	12±3	3.19±0.04	3.299
Co2	O6	1	9±5	2.01±0.02	4±1	1.836±0.008	2.027
	O1	1	9±5	2.05±0.02	4±1	1.872±0.009	2.067
	O5	1	6±2	2.08±0.02	4±1	1.96±0.03	2.105
	N1	1	6±2	2.17±0.02	4±1	2.12±0.02	2.129
	O1	1	9±2	2.18±0.02	4±1	1.936±0.009	2.138
	O3	1	9±2	2.22±0.02	4±1	1.971±0.009	2.176
	Co2	1	2.3±0.8	3.16±0.01	12±3	3.06±0.03	3.165
	Co1.1	1	2.3±0.8	3.21±0.01	12±3	3.10±0.04	3.207
	Co1.2	1	2.3±0.8	3.30±0.01	12±3	3.19±0.04	3.299

r = distances between atom 1-atom 2; $\sigma^2/\text{\AA}^2$ = Debye-Waller factor; N = scattering path

(1) Stern, E. A. *Phys. Rev. B* **1993**, 48, 9825-9827.

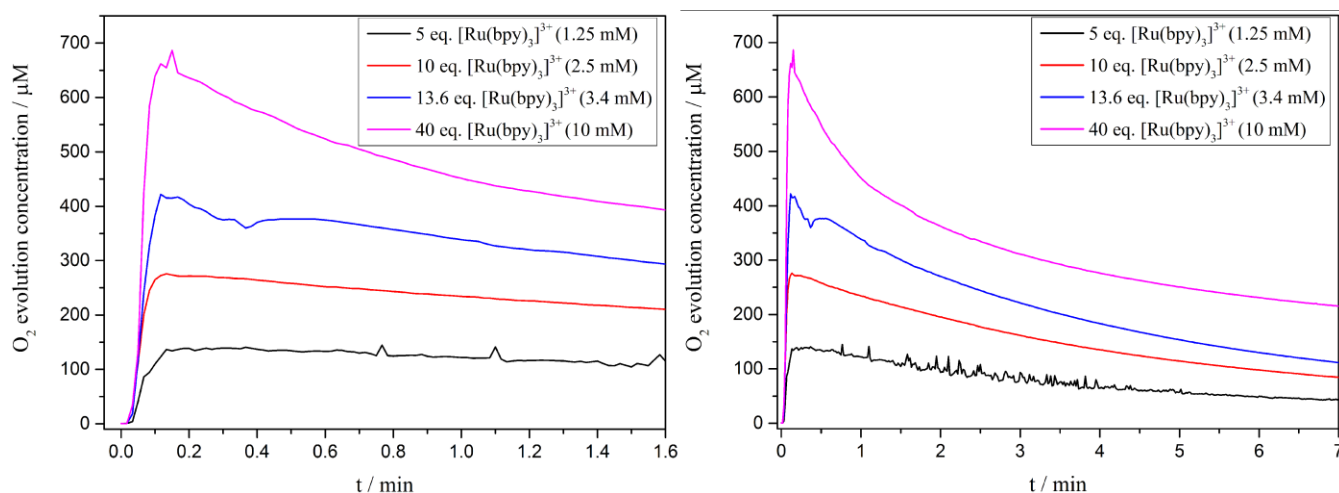


Figure S25. Clark electrode kinetics of chemical water oxidation catalyzed by 250 μM $\text{Co}_4\text{O}_4\text{-dpk}$ with various amounts of $[\text{Ru}(\text{bpy})_3](\text{ClO}_4)_3$ oxidant.

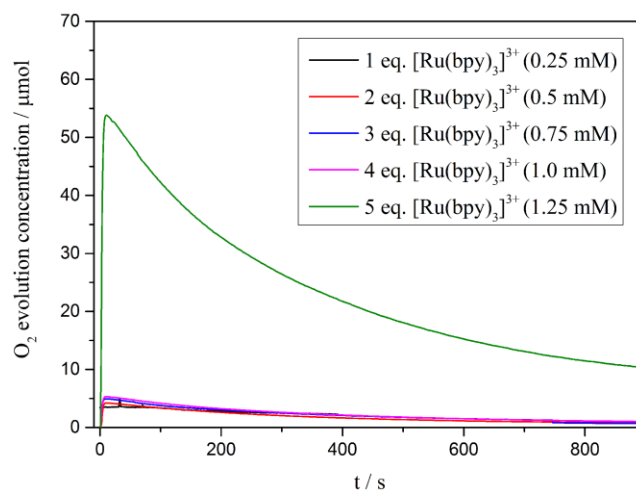


Figure S26. Clark electrode kinetics of chemical water oxidation catalyzed by 250 μM $\text{Co}_4\text{O}_4\text{-dpk}$ with increasing equivalents of $[\text{Ru}(\text{bpy})_3](\text{ClO}_4)_3$ oxidant (after subtraction of background O_2 evolution in the absence of catalyst).

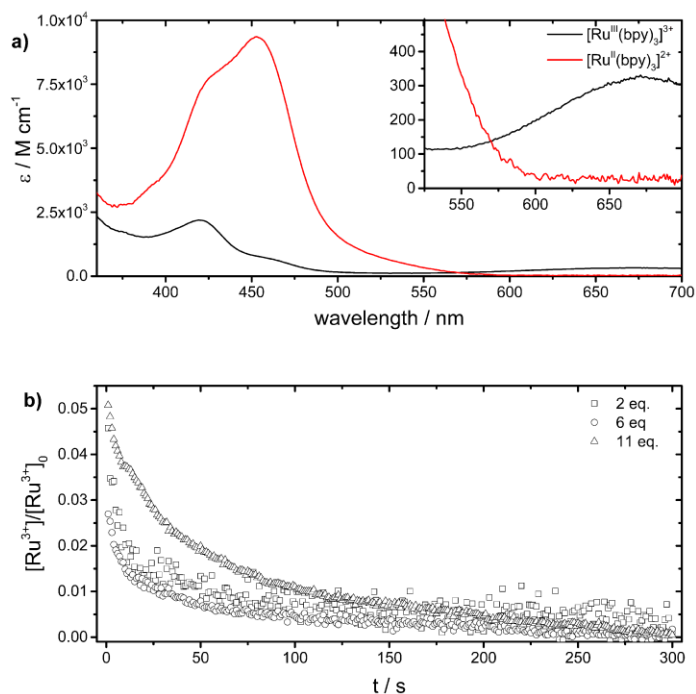


Figure S27. (a) UV/vis spectrum of $[\text{Ru}(\text{bpy})_3](\text{ClO}_4)_3$ in 0.5 M H_2SO_4 (black curve) and in pH 8.5 borate buffer (red curve) after 30 min ageing time; (b) UV/vis kinetics of 100 μM $\text{Co}_4\text{O}_4\text{-dpk}$ catalyzed chemical water oxidation with various amounts of $[\text{Ru}(\text{bpy})_3](\text{ClO}_4)_3$ oxidant ($[\text{Ru}(\text{bpy})_3]^{3+}$ concentrations were determined from the absorption at 675 nm).

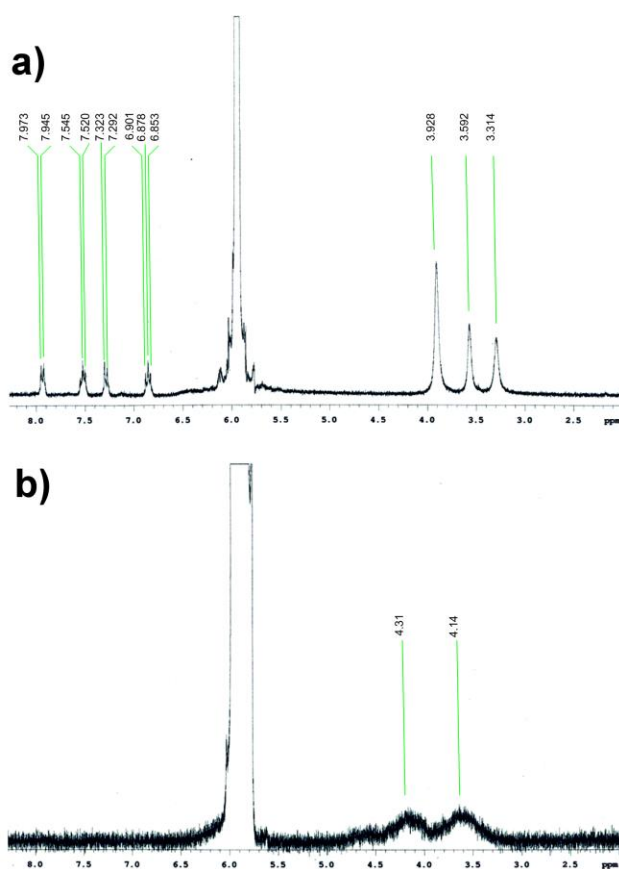


Figure S28. ^1H NMR spectra of (a) $[(\text{NH}_3)_4\text{Co(III)sal}]\text{Cl}$ precursor and (b) $[(\text{NH}_3)_4\text{Co(IV)sal-NO}_2]\text{ClO}_3$ reference.

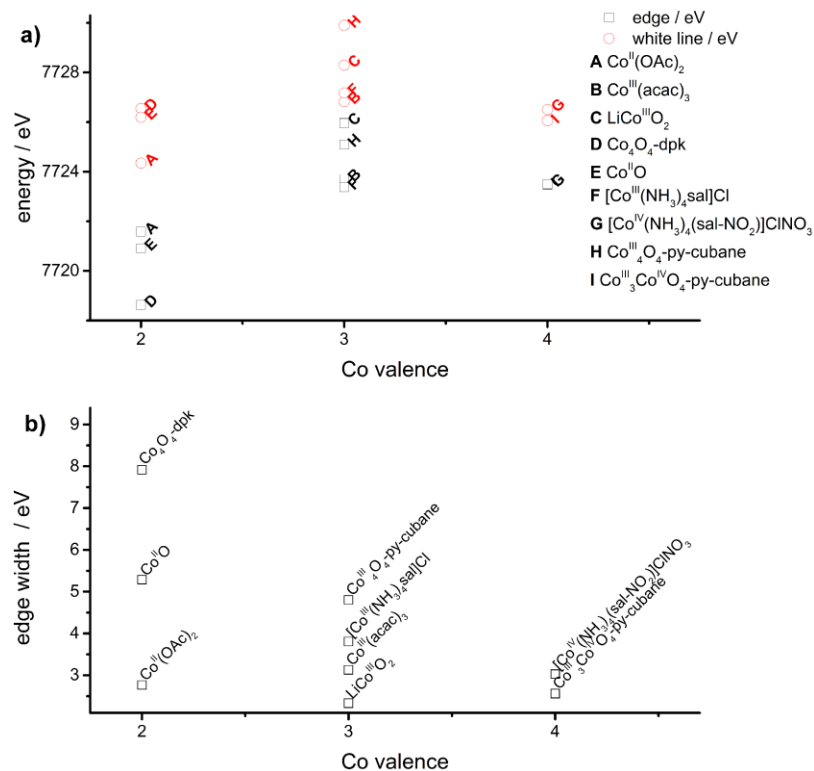


Figure S29. (a) Comparison of the edge position and white line for different cobalt containing samples; (b) corresponding edge width (difference of white line and edge position).

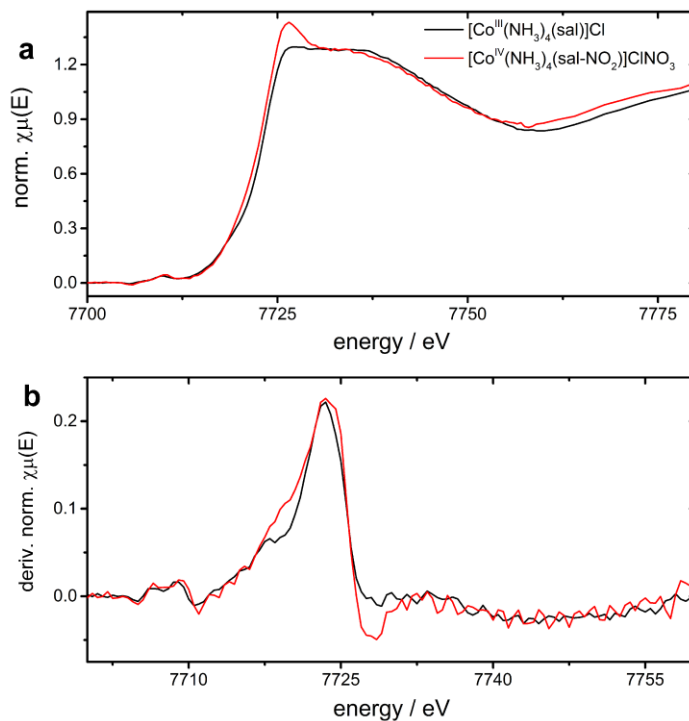


Figure S30. Normalized XANES spectra of $[(\text{NH}_3)_4\text{Co}(\text{III})\text{sal}]\text{Cl}$ and $[(\text{NH}_3)_4\text{Co}(\text{IV})\text{sal-NO}_2]\text{ClO}_3$ (a) and 1st derivative of the normalized spectra (b).

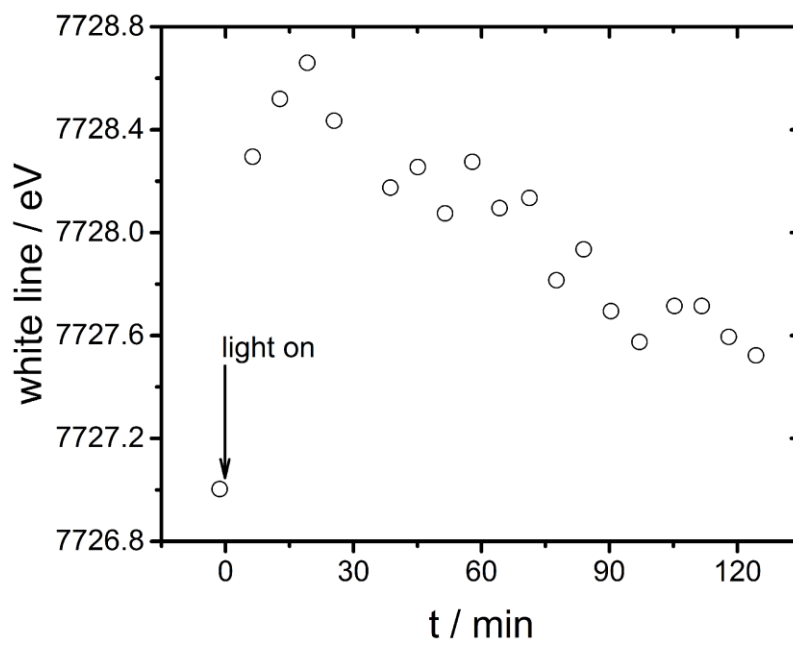


Figure S31. White line positions of XANES monitoring of 100 μM $\text{Co}_4\text{O}_4\text{-dpk}$ in pH 8.5 borate buffer.

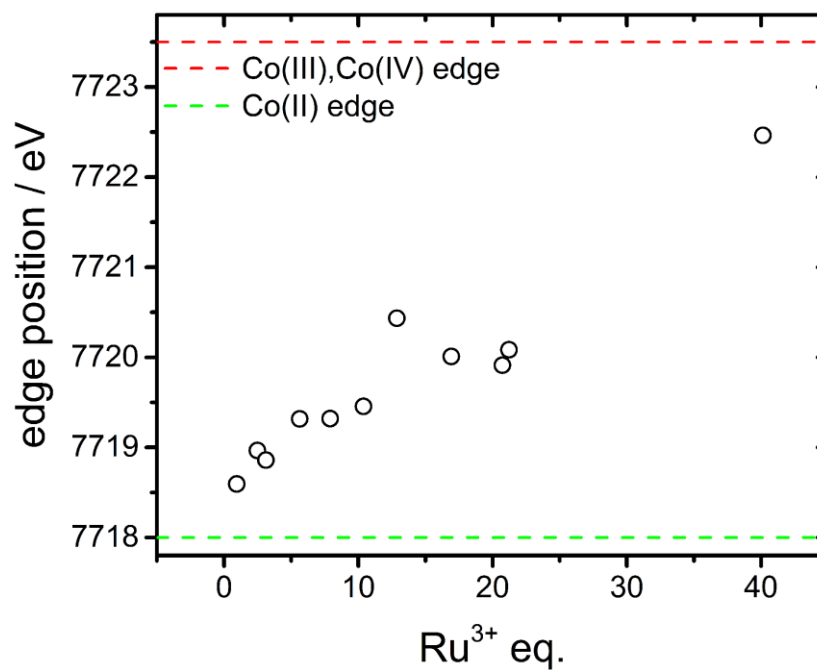


Figure S32. Cobalt K-edge position for 250 μM $\text{Co}_4\text{O}_4\text{-dpk}$ upon chemical oxidation with various amounts of $[\text{Ru}(\text{bpy})_3](\text{ClO}_4)_3$ at 40 K.

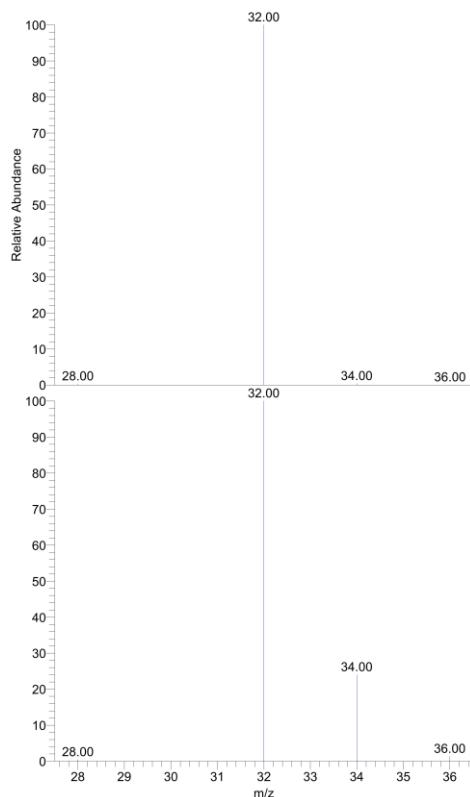


Figure S33. Electron impact ionization mass spectra of the gas sample evolved during the irradiation of H_2^{16}O (top) and H_2^{18}O (10.8 at% ^{18}O) (bottom) containing borate buffer solutions (pH 8.5, 80 mM) with 100 μM of **Co₄O₄-dpk** cubane, 1 mM $[\text{Ru}(\text{bpy})_3]\text{Cl}_2$, and 5 mM $\text{Na}_2\text{S}_2\text{O}_8$.

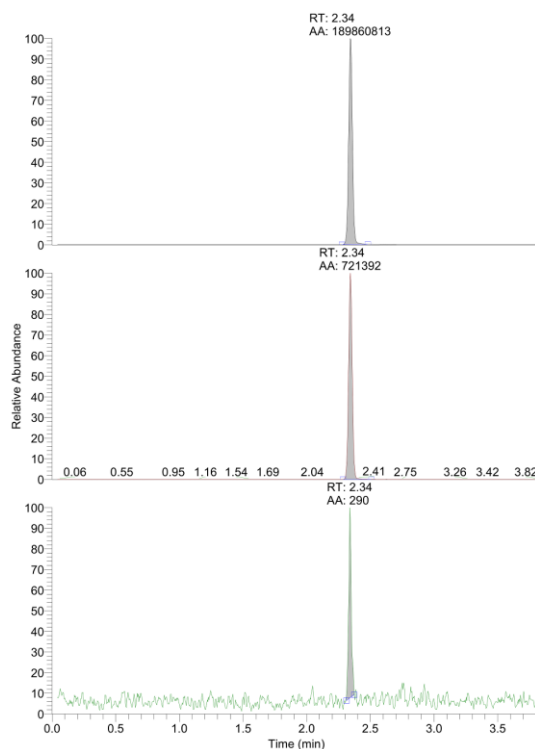


Figure S34. GC data of $^{32}\text{O}_2$ (top), $^{34}\text{O}_2$ (middle), and $^{36}\text{O}_2$ (bottom) evolved during the irradiation of a H_2^{16}O containing borate buffer (pH 8.5, 80 mM) solution with 100 μM of **Co₄O₄-dpk** cubane, 1 mM $[\text{Ru}(\text{bpy})_3]\text{Cl}_2$, and 5 mM $\text{Na}_2\text{S}_2\text{O}_8$.

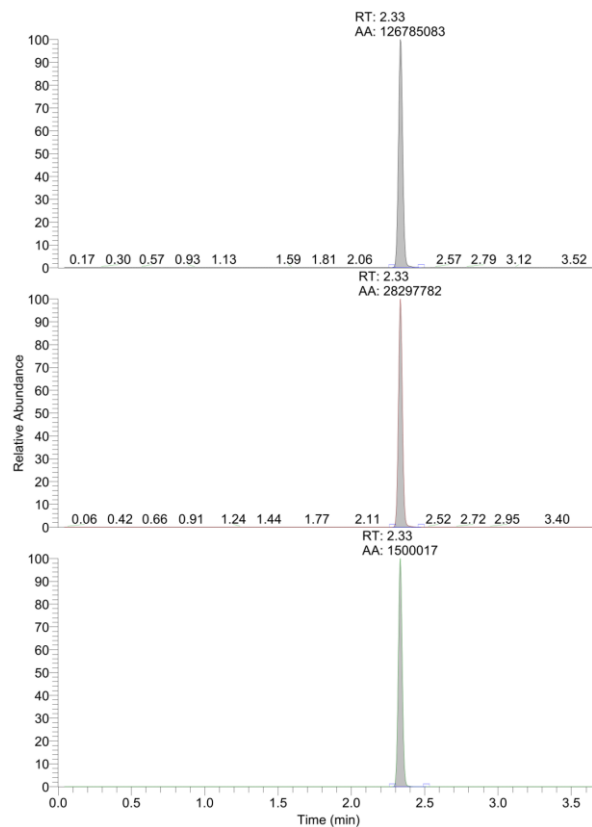


Figure S35. GC data of $^{32}\text{O}_2$ (top), $^{34}\text{O}_2$ (middle), and $^{36}\text{O}_2$ (bottom) evolved during the irradiation of a H_2^{18}O (10.8 at% ^{18}O) containing borate buffer (pH 8.5, 80 mM) solution with 100 μM of **Co₄O₄-dpk** cubane, 1 mM $[\text{Ru}(\text{bpy})_3]\text{Cl}_2$, and 5 mM $\text{Na}_2\text{S}_2\text{O}_8$.

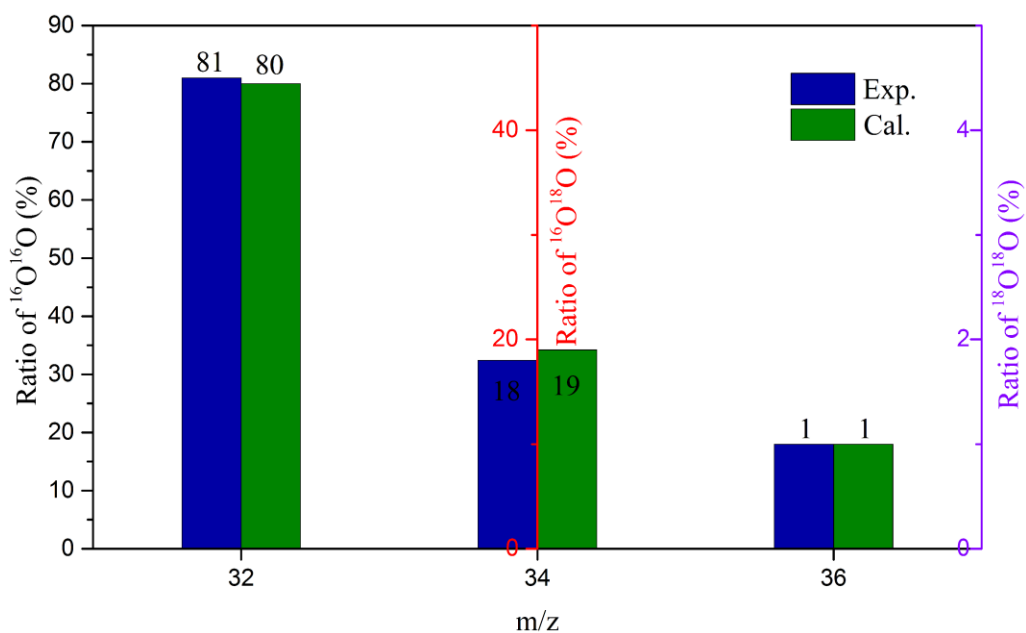


Figure S36. Experimental and theoretical ratios of $^{16}\text{O}^{16}\text{O}$, $^{16}\text{O}^{18}\text{O}$, and $^{18}\text{O}^{18}\text{O}$ evolved during the irradiation of a H_2^{18}O (10.8 at% ^{18}O) containing borate buffer (pH 8.5, 80 mM) solution with 100 μM of **Co₄O₄-dpk** cubane, 1 mM $[\text{Ru}(\text{bpy})_3]\text{Cl}_2$, and 5 mM $\text{Na}_2\text{S}_2\text{O}_8$.

Current research survey: Mixed Co/Ni-containing water oxidation catalysts

Table S8. Literature survey of mixed Co/Ni-containing water oxidation catalyst types (selection)

Co/Ni-WOC Test method	Type/	Compound	Hypotheses for Co/Ni interactions	Ref.
		Ni _x Co _{3-x} O ₄ spinels	Ni modulates electronic properties of active sites and thus modifies adsorption energies of intermediates	[1]
		Ni _x Co _{3-x} O _{4-y}	Nonstoichiometry together with low coordination metal sites both lower the HO [•] adsorption energy, while non-homogeneous surface further promotes activity	[2]
		Ni _x Co _{1-x} O	Reduction of the work function of (001) and (100) surfaces with increasing Co contents	[3]
		Ni-Co LDH nanosheets	Beneficial (tetrahedral) Ni ³⁺ surface enrichment facilitates formation of NiOOH active sites	[4]
		NiCo ₂ O ₄ nanowire arrays	General promoting effect of highly exposed high-index facets of the nanowires	[5]
		Ni _{1+x} Co _{2-x} O ₄ series	Strong dependence of redox couples' site occupancies and resulting performances on the preparation method, irreversible Ni ³⁺ formation has to be avoided	[6]
		Preparative/morphological progress		
		Ni _x Co _y O ₄	Supported on Co/N decorated graphene as a composite	[7]
		NiCo-LDH	Nanosheet arrays grown on Ni foam	[8]
		NiCo ₂ O ₄	Nanowire OER component of Ni/Co OER/HER device	[9]
		NiCo ₂ O ₄	Hollow-urchin morphologies, superior over nanoparticles	[10]
		Ni _x Co _{3-x} O ₄ nanowires	Conversion into NiCo/NiCoO _x HER catalysts for overall water splitting devices	[11]
		Ni-rich Ni-Co oxide layers	Nanoporous materials through anodization	[12]
		CoNi hydroxide nanosheets	Deposition on Ni foam equipped with stabilizing Ni nanocones	[13]
Heterogeneous/ Photoelectrochemical		NiCoO _x film (co-sputtered)	Lower resistance, enhanced chemisorption properties	[14]
Heterogeneous/ Theoretical studies		β-NiOOH with Co	Optimized binding energies of intermediates on all sites reduce overpotential of water oxidation	[15]
Heterogeneous/ Chemical oxidation		No records found to date		
Molecular/ Electrochemical		No records found to date		
Molecular/ Photochemical		No records found to date		
Molecular/ Chemical oxidation		No records found to date		

Table S8 provides a preliminary overview of reports on mixed Co/Ni-oxide based water oxidation catalysts based on literature research. Although this short survey is far from complete, it clearly demonstrates that the majority of Co/Ni-oxide WOCs have been assessed with electrochemical methods. Mostly, they outperformed their binary counterparts in electrochemical water oxidation. In sharp contrast, no reports on molecular Co/Ni-WOCs were found in different databases to date (within a reasonable search time interval).

This trend impressively highlights the significant dependence of the performance assessment on the applied oxidation method, as has been pointed out in recent fundamental studies.¹⁶ Surprisingly, almost no data are available for the corresponding photochemical water oxidation performance of the excellent Co/Ni electrocatalysts listed above. Moreover, molecular Co/Ni-WOCs appear to remain rather unexplored to date.

Among the growing number of studies on electrochemical water oxidation with Co/Ni-containing oxide WOCs (further non-oxide Co/Ni-systems have been omitted for the sake of brevity in Table S8), the interpretation of the observed Co-Ni synergisms remains somewhat controversial. Most hypotheses are focused on improved general surface properties³ and on the enhancement of active sites with respect to favorable intermediate adsorption energies.^{1,2} Although theoretical studies support these hypotheses, they also demonstrate that modeling results may depend on the selected surface unit cell size.¹⁵

All in all, most Co/Ni synergism models for solid state electrochemical WOCs emphasize statistical surface and bulk-related effects (such as enhanced conductivity). To the best of our knowledge, no investigations of Co/Ni interaction on the molecular level have been performed that are comparable to such benchmark studies on Co₃O₄.¹⁷ This renders new molecular heterometallic Co/Ni-WOCs indispensable targets to understand important performance/mechanistic discrepancies between different catalyst and assay types. The present {Co_xNi_{4-x}O₄} cubanes offer the unique opportunity to study mixed edge-site motifs within a confined and well-defined ligand environment.

All in all, the following questions of general interest emerge from the present state-of-the-art for Co/Ni-WOCs:

- (1) Do their electro- and (photo)chemical pathways differ fundamentally?
- (2) Do molecular and heterogeneous compounds display different oxygen evolution mechanisms?
- (3) Most important conclusion from (1) & (2):

What are the consequences for the unification of molecular and heterogeneous WOC design concepts?

- (1) Abidat, I.; Morais, C.; Comminges, C.; Canaff, C.; Rousseau, J.; Guignard, N.; Napporn, T. W.; Habrioux, A.; Kokoh, K. B. *J. Mater. Chem. A* **2017**, 5, 7173–7183.
- (2) Antony, R. P.; Satpati, A. K.; Bhattacharyya, K.; Jagatap, B. N. *Adv. Mater. Interfaces* **2016**, 3, 1600632.
- (3) Fominykh, K.; Tok, G. C.; Zeller, P.; Hajiyani, H.; Miller, T.; Döblinger, M.; Pentcheva, R.; Bein, T.; Fattakhova-Rohlfing, D. *Adv. Funct. Mater.* **2017**, 27, 1605121.
- (4) Wang, H.-Y.; Hsu, Y.-Y.; Chen, R.; Chan, T.-S.; Chen, H. M.; Liu, B. *Adv. Energy Mater.* **2015**, 5, 1500091.
- (5) Yu, X.; Sun, Z.; Yan, Z.; Xiang, B.; Liu, X.; Du, P. *J. Mater. Chem. A* **2014**, 2, 20823–20831.
- (6) Chanda, D.; Hnát, J.; Bystron, T.; Paidar, M.; Bouzek, K. *J. Power Sources* **2017**, 347, 247–258.
- (7) Hao, Y.; Xu, Y.; Liu, J.; Sun, X. *J. Mater. Chem. A* **2017**, 5, 5594–5600.
- (8) Jiang, J.; Zhang, A.; Li, L.; Ai, L. *J. Power Sources* **2015**, 278, 445–451.
- (9) Peng, Z.; Jia, D.; Al-Enizi, A. M.; Elzatahry, A. A.; Zheng, G. *Adv. Energy Mater.* **2015**, 5, 1402031.
- (10) Wang, J.; Qiu, T.; Chen, X.; Lu, Y.; Yang, W. *J. Power Sources* **2014**, 268, 341–348.
- (11) Yan, X.; Li, K.; Lyu, L.; Song, F.; He, J.; Niu, D.; Liu, L.; Hu, X.; Chen, X. *ACS Appl. Mater. Interf.* **2016**, 8, 3208–3214.
- (12) Yang, Y.; Fei, H.; Ruan, G.; Xiang, C.; Tour, J. M. *ACS Nano* **2014**, 8, 9518–9523.
- (13) Yoon, S.; Yun, J.-Y.; Lim, J.-H.; Yoo, B. *J. Alloys Comp.* **2017**, 693, 964–969.
- (14) Bae, D.; Mei, B.; Frydendal, R.; Pedersen, T.; Seger, B.; Hansen, O.; Vesborg, P. C. K.; Chorkendorff, I. *ChemElectroChem* **2016**, 3, 1546–1552.
- (15) Costanzo, F. *Phys. Chem. Chem. Phys.* **2016**, 18, 7490–7501.
- (16) Pokhrel, R.; Goetz, M. K.; Shaner, S. E.; Wu, X.; Stahl, S. S. *J. Am. Chem. Soc.* **2015**, 137, 8384–8387.
- (17) Zhang, M.; Respinis, M. de; Frei, H. *Nature Chem.* **2014**, 6, 362–367.

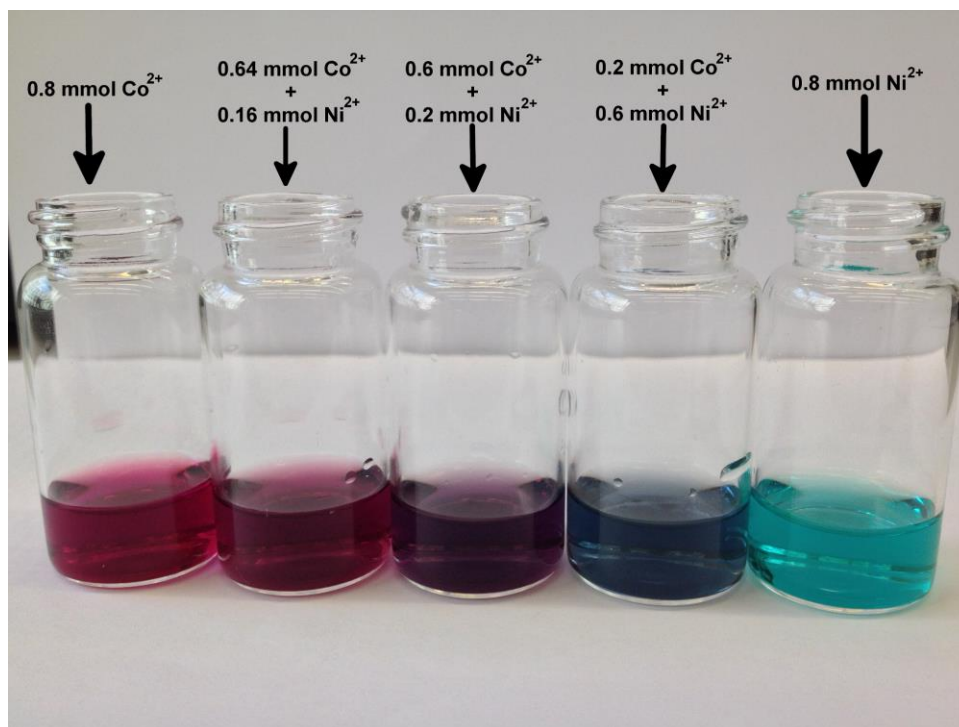


Figure S37. Synthetic solutions of **Co₄O₄-dpk**, **Co_xNi_{4-x}O₄-dpk** series, and **Ni₄O₄-dpk** (left to right).

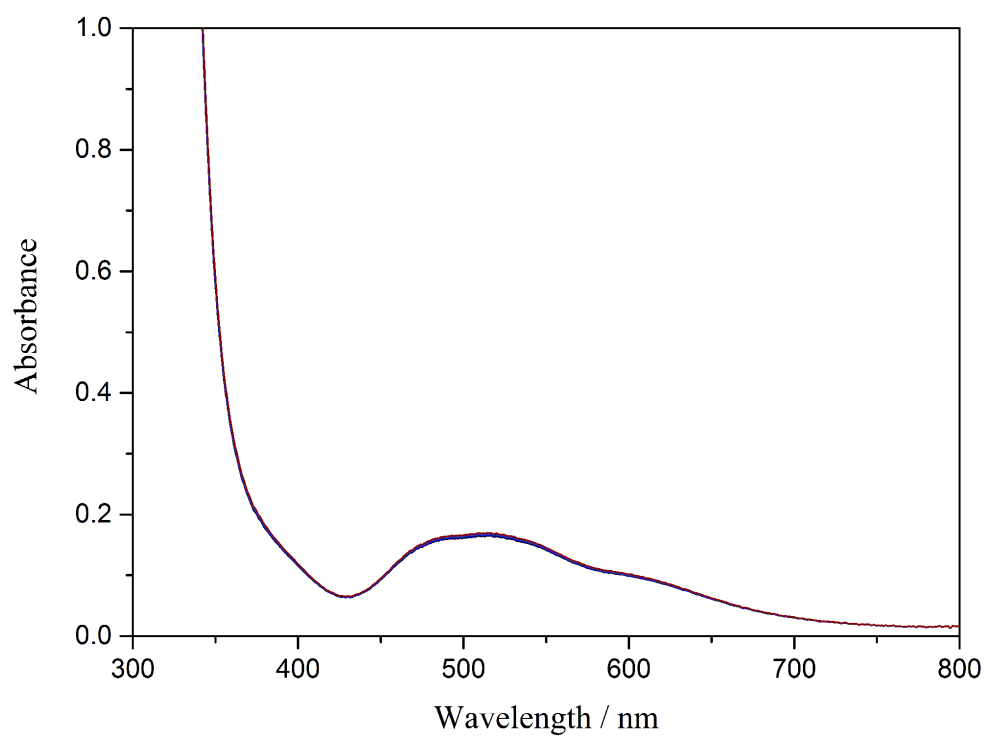


Figure S38. Time dependent UV/vis spectra of 1.5 mM **Co_{2.65}Ni_{1.35}O₄-dpk** cubane in pH 8.5, 80 mM borate buffer solution over 2 h.

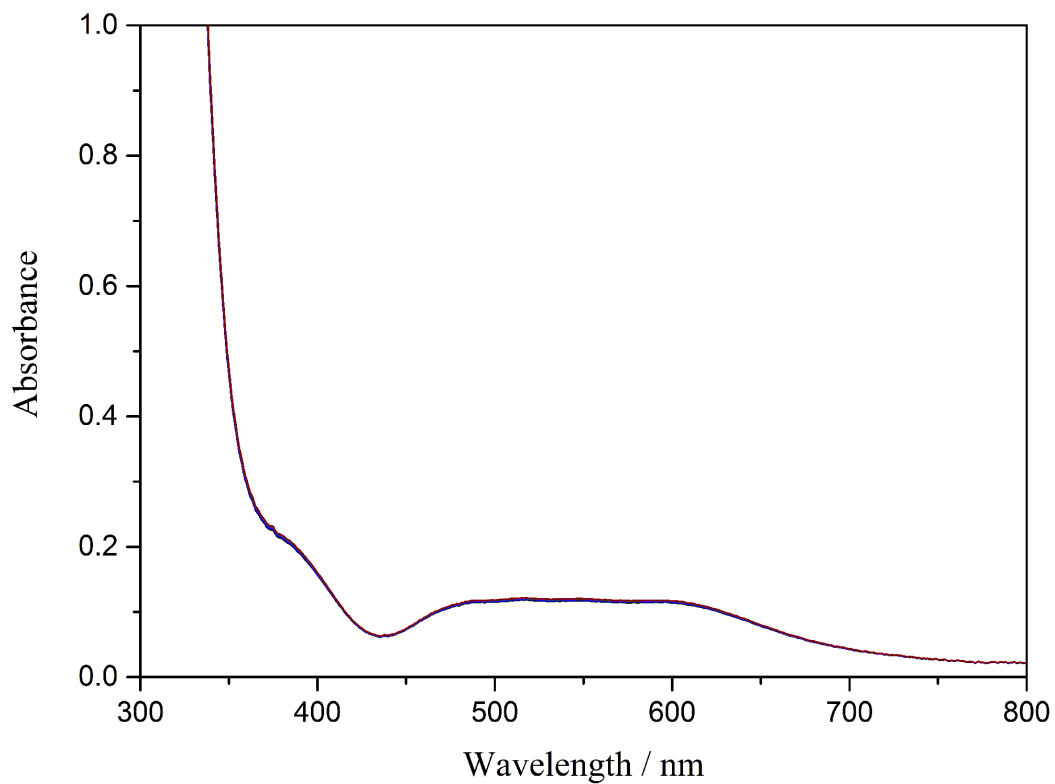


Figure S39. Time dependent UV/vis spectra of 1.5 mM $\text{Co}_{2.05}\text{Ni}_{1.95}\text{O}_4\text{-dpk}$ cubane in pH 8.5, 80 mM borate buffer solution over 2 h.

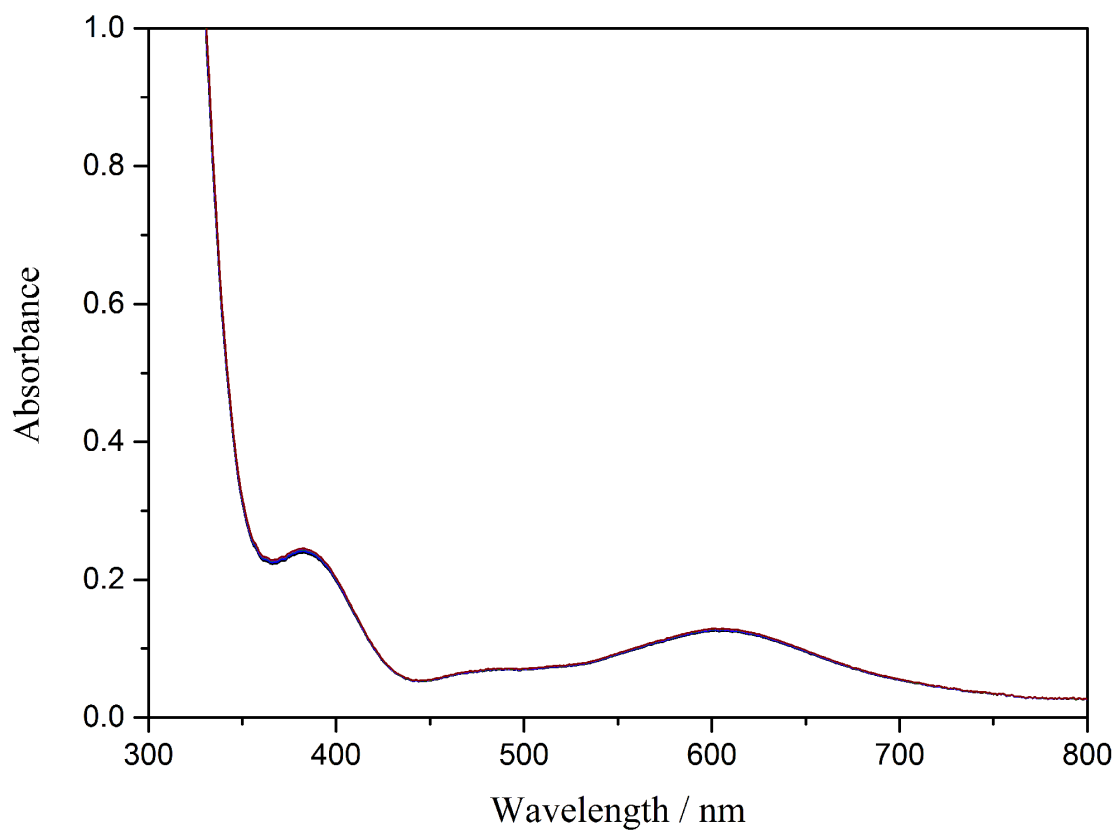


Figure S40. Time dependent UV/vis spectra of 1.5 mM $\text{Co}_{1.15}\text{Ni}_{2.85}\text{O}_4\text{-dpk}$ cubane in pH 8.5, 80 mM borate buffer solution over 2 h.

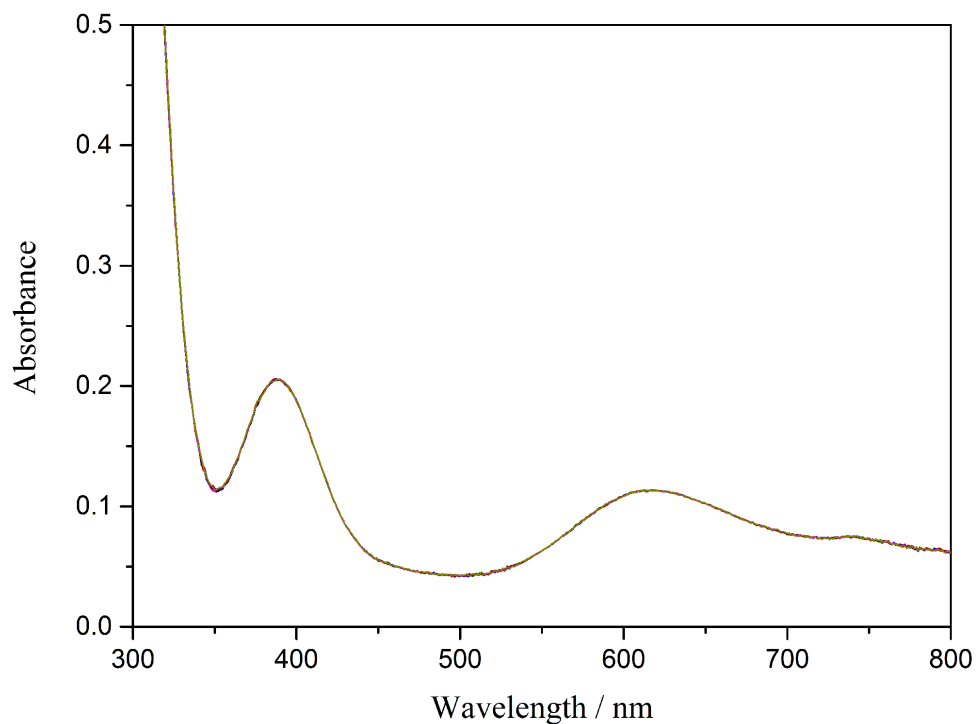


Figure S41. Time dependent UV/vis spectra of 3.0 mM $\text{Ni}_4\text{O}_4\text{-dpk}$ cubane in pH 8.5, 80 mM borate buffer solution over 2 h.

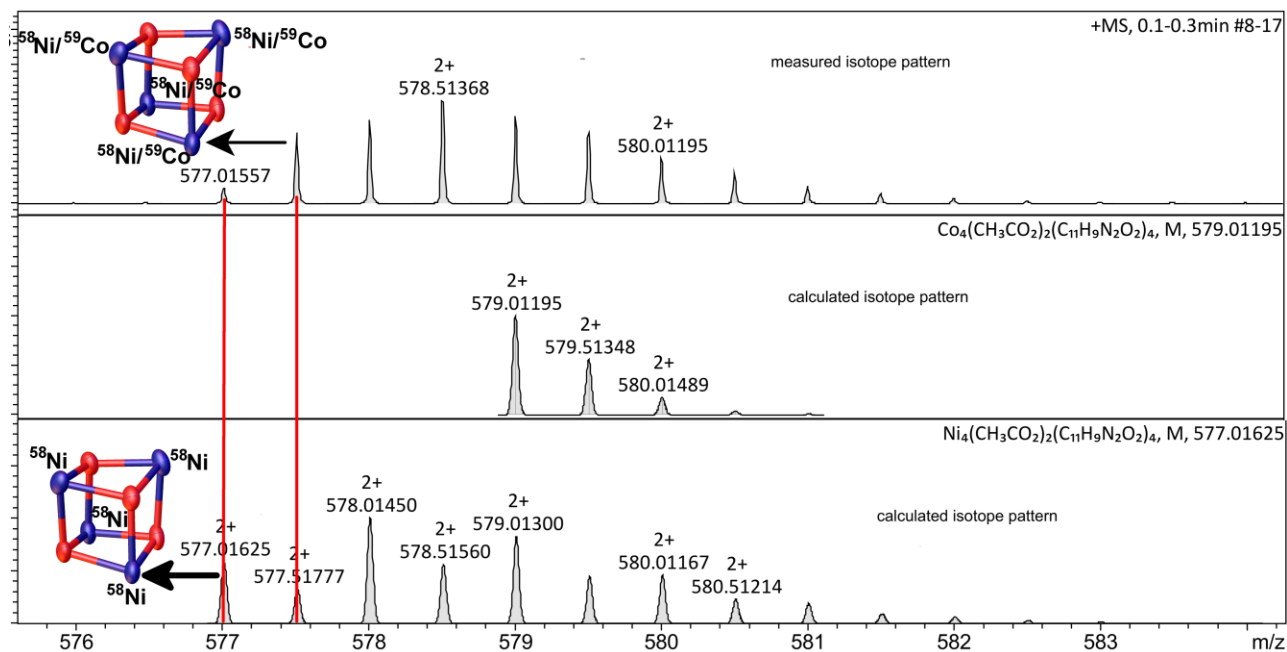


Figure S42. HR-ESI-MS spectra comparison of $\text{Co}_4\text{O}_4\text{-dpk}$, $\text{Ni}_4\text{O}_4\text{-dpk}$, and $\text{Co}_{1.15}\text{Ni}_{2.85}\text{O}_4\text{-dpk}$ in the m/z range of 576-583.

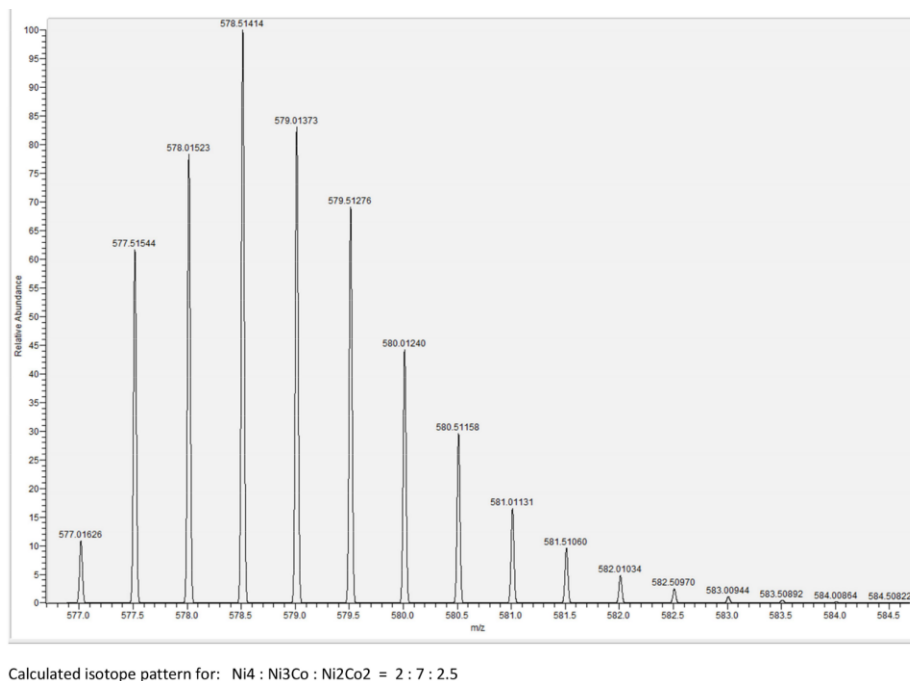


Figure S43. Calculated MS spectrum of **Co_{1.15}Ni_{2.85}O₄-dpk** in the m/z range of 577.0-584.5.

Table S9. Photocatalytic water oxidation performance of 100 μM of **Co₄O₄-dpk** and of the **Co_xNi_{4-x}O₄-dpk** series in pH 8.5 borate buffer solution (80 mM).

Catalyst	O ₂ area	N ₂ area	O ₂ /μmol	^a O ₂ yield	^b TON	^c TOF / s ⁻¹
Co₄O₄-dpk	1488.8	55.4	16.0	80%	20.0	0.24
Co_{2.80}Ni_{1.20}O₄-dpk	1185.4	32.3	12.8	64%	16.0	0.21
Co_{2.65}Ni_{1.35}O₄-dpk	1182.2	26.2	12.8	64%	16.0	0.21
Co_{2.05}Ni_{1.95}O₄-dpk	782.4	9.9	8.6	43%	10.8	0.14
Co_{1.15}Ni_{2.85}O₄-dpk	502.8	15.1	5.5	28%	6.9	0.10

^aO₂ yield = 2 × mole of O₂ (GC)/mole of Na₂S₂O₈. ^bTON = mole of O₂ (GC)/mole of catalyst. ^cTOF_{initial} = initial concentration of O₂ evolution (Clark electrode kinetics in 60 s)/catalyst concentration. Conditions: 470 nm LED; 100 μM of **Co₄O₄-dpk**; 1 mM [Ru(bpy)₃]Cl₂; 5 mM Na₂S₂O₈; standard deviation of molar O₂ yields: ca. 3%.

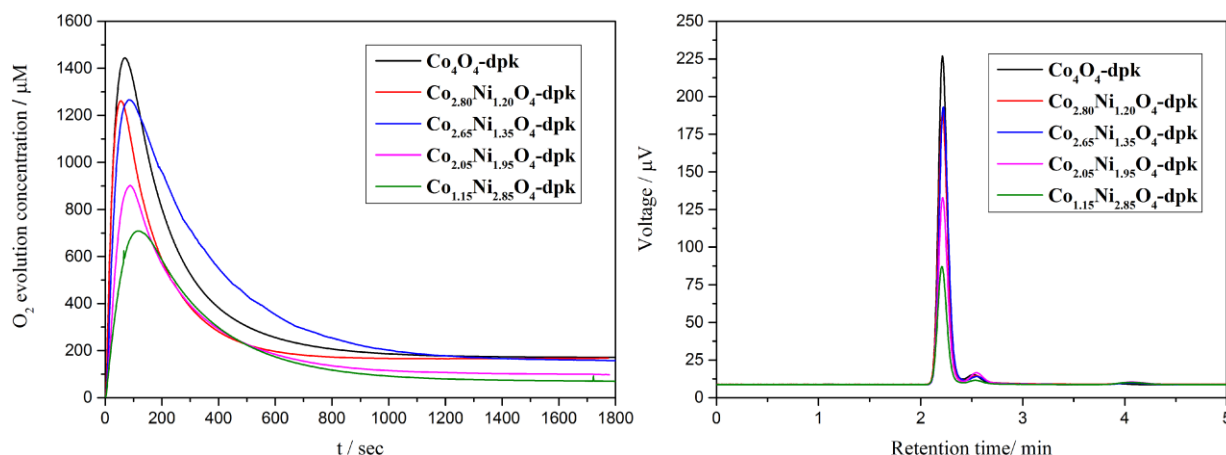


Figure S44. Clark electrode kinetics (a) and GC measurement (b) of visible light-driven water oxidation catalyzed by 100 μM **Co₄O₄-dpk** (black) and the **Co_xNi_{4-x}O₄-dpk** series (conditions: 470 nm LED; 1 mM [Ru(bpy)₃]Cl₂; 5 mM Na₂S₂O₈; pH 8.5, 80 mM borate buffer), respectively.

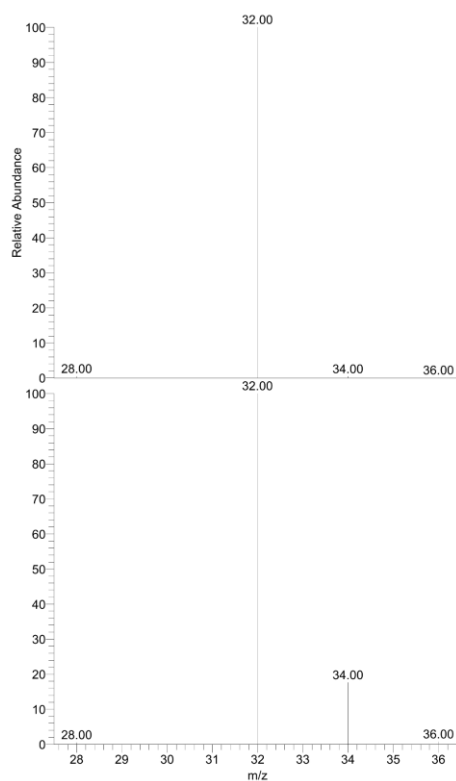


Figure S45. Electron impact ionization mass spectra of the gas sample evolved during the irradiation of H_2^{16}O (top) and H_2^{18}O (8.3 at% ^{18}O) (bottom) containing borate buffer solutions (pH 8.5, 80 mM) with 100 μM of **Co_{2.65}Ni_{1.35}O₄-dpk** cubane, 1 mM $[\text{Ru}(\text{bpy})_3]\text{Cl}_2$, and 5 mM $\text{Na}_2\text{S}_2\text{O}_8$.

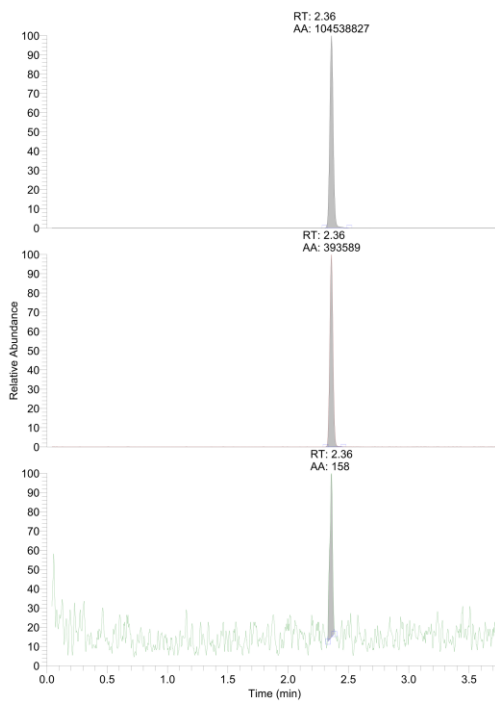


Figure S46. GC data of $^{32}\text{O}_2$ (top), $^{34}\text{O}_2$ (middle), and $^{36}\text{O}_2$ (bottom) evolved during the irradiation of a H_2^{16}O containing borate buffer (pH 8.5, 80 mM) solution with 100 μM of **Co_{2.65}Ni_{1.35}O₄-dpk** cubane, 1 mM $[\text{Ru}(\text{bpy})_3]\text{Cl}_2$, and 5 mM $\text{Na}_2\text{S}_2\text{O}_8$.

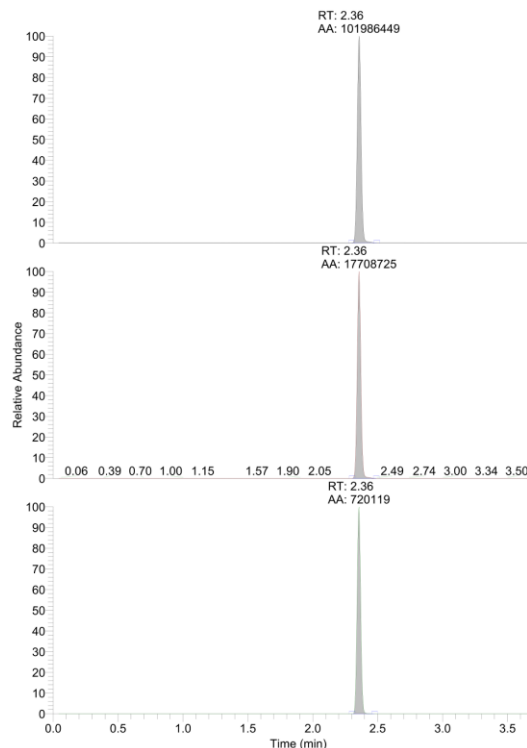


Figure S47. GC data of $^{32}\text{O}_2$ (top), $^{34}\text{O}_2$ (middle), and $^{36}\text{O}_2$ (bottom) evolved during the irradiation of a H_2^{18}O (8.3 at% ^{18}O) containing borate buffer (pH 8.5, 80 mM) solution with 100 μM of $\text{Co}_{2.65}\text{Ni}_{1.35}\text{O}_4\text{-dpk}$ cubane, 1 mM $[\text{Ru}(\text{bpy})_3]\text{Cl}_2$, and 5 mM $\text{Na}_2\text{S}_2\text{O}_8$.

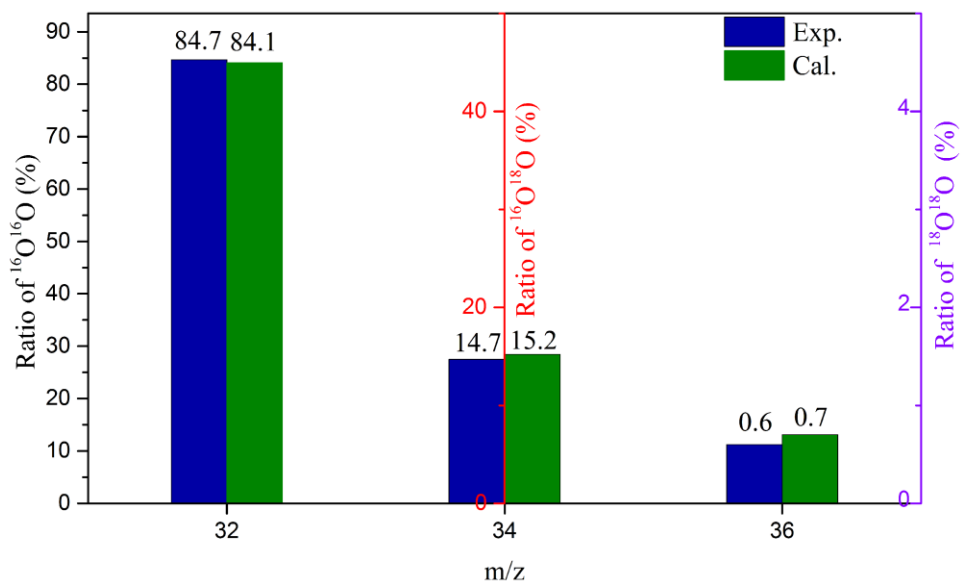


Figure S48. Experimental and theoretical ratios of $^{16}\text{O}^{16}\text{O}$, $^{16}\text{O}^{18}\text{O}$, and $^{18}\text{O}^{18}\text{O}$ evolved during the irradiation of a H_2^{18}O (8.3 at% ^{18}O) containing borate buffer (pH 8.5, 80 mM) solution containing 100 μM of $\text{Co}_{2.65}\text{Ni}_{1.35}\text{O}_4\text{-dpk}$ cubane, 1 mM $[\text{Ru}(\text{bpy})_3]\text{Cl}_2$, and 5 mM $\text{Na}_2\text{S}_2\text{O}_8$.

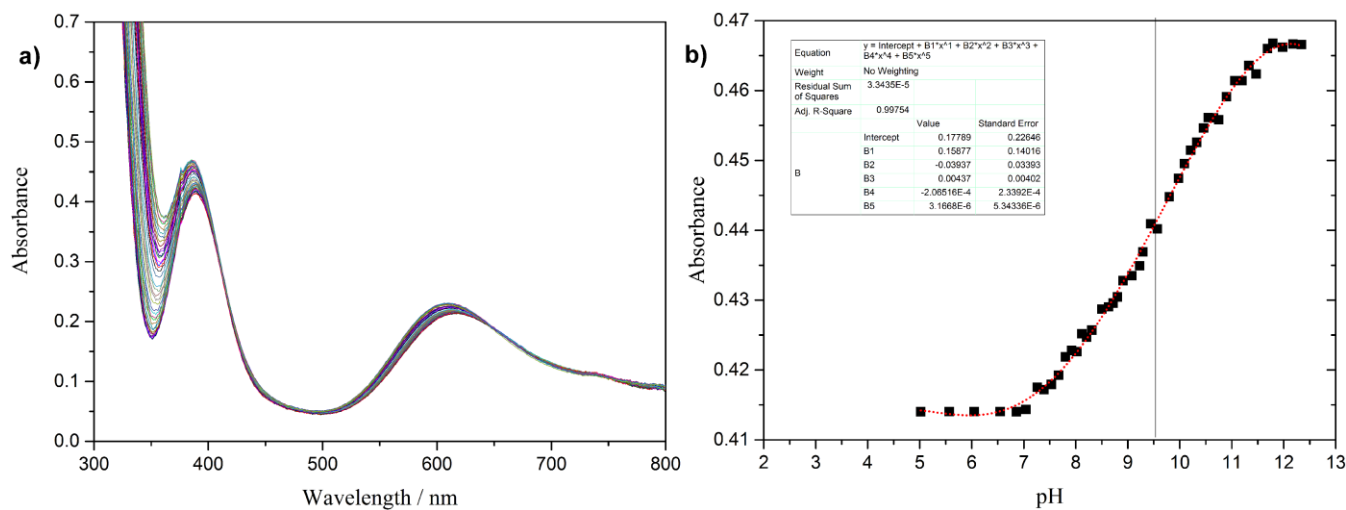


Figure S49. (a) pH dependent UV/vis spectra of 7 mM of $\text{Ni}_4\text{O}_4\text{-dpk}$ cubane; (b) representative plot of the absorbance at 389 nm vs. pH.

Computational Settings

Density functional theory-based molecular dynamics (DFT-MD) simulations were performed using the QUICKSTEP program¹ as implemented in the CP2K package,² which uses a mixed Gaussian and plane wave scheme with the wave functions expanded in terms of a Gaussian basis set and the charge density represented via an auxiliary plane wave basis. The computational model contained the cubane (**Co₄O₄-dpk**) (or a deprotonated variant thereof) and 208 and 452 water molecules, respectively, in a periodic cubic box, and was first run in the NPT ensemble where the temperature of the system was stepwise increased from 50 K to 300 K. Furthermore, the behavior of the pressure was monitored by changing the box size in the NVT ensemble at 300 K. With the final box size of 18.7340³ Å³ for the small system and 24.180³ Å³ for the large one, we equilibrated all systems for 10-15 ps in the NVT ensemble using a time step of 0.5 fs. The temperature was held close to 300 K using CSV thermostat (canonical sampling through velocity rescaling)³ with a time constant of 10 fs. For the production runs, we used the NVT ensemble and the CSV thermostat with a time constant of 50 fs and sampled for additional 20 ps using a time step of 0.5 fs. The introduction of a negative background charge allowed us to neutralize the otherwise charged system. While the background charge is an artificial feature, it is known to introduce less bias than explicit counter ions in the infinite dilution limit.⁴ We assumed a high spin configuration as well as ferromagnetic coupling for all four cobalt centers. Unless otherwise stated, the generalized gradient approximation (GGA) exchange-correlation (XC) functional Perdew-Burke-Ernzerhof (PBE)⁵ was used. We employed the DZVP-MOLOPT-GTH basis sets,⁶ a 500 Ry cutoff for the auxiliary plane wave expansion of the charge density, and the Goedecker-Teter-Hutter (GTH)^{7,8} norm-conserving pseudopotentials to represent the core electrons. Kohn-Sham and overlap matrix elements smaller than $\epsilon_{\text{default}} = 10^{-12}$ were neglected, and the convergence criterion for the electronic gradient (largest element of the gradient) was set to $\epsilon_{\text{SCF}} = 1 \cdot 10^{-6}$ (small system) and $\epsilon_{\text{SCF}} = 5 \cdot 10^{-6}$ (large system). In addition we applied the D3 dispersion correction by Grimme et al.⁹ to correct for the overstructuring of water observed with GGA-XC functionals. For the production runs described above, a drift in the total energy of 10⁻⁵ a.u./ps/atom was found. Comparing the two different system sizes, we found that the additional water layers did not significantly change the behavior of the cubane (see Table S8). In order to save computational resources, we performed longer equilibration runs (> 10 ps) only for the smaller system.

Table S10. Description of the oxygen-oxygen radial distribution function $g_{\text{OO}}(r)$ in terms of position (in Å) of the first maximum (r_1^{max}), the first minimum (r_1^{min}), and the second maximum (r_2^{max}) for the neutral cubane (**Co₄O₄-dpk**), compared to reference calculations of a box containing 64 water molecules using the PBE functional as well as a self-consistent (SC) dispersion correction based on Tkatchenko-Scheffler (TS-vdW) density dependent van der Waals/dispersion functional.¹⁰

	T (K)	r_1^{max}	r_1^{min}	r_2^{max}
PBE-D3 (452 solvent water molecules)	300	2.75	3.25	4.35
PBE-D3 (208 solvent water molecules)	300	2.75	3.17	4.18
PBE _(bulk water) ¹¹	300	2.69	3.28	4.44
PBE-TS-vdW(SC) _(bulk water) ¹¹	300	2.71	3.27	4.40
Experiment ¹²	295	2.80	3.45	4.50
Experiment ¹³	295	2.76	3.42	4.43

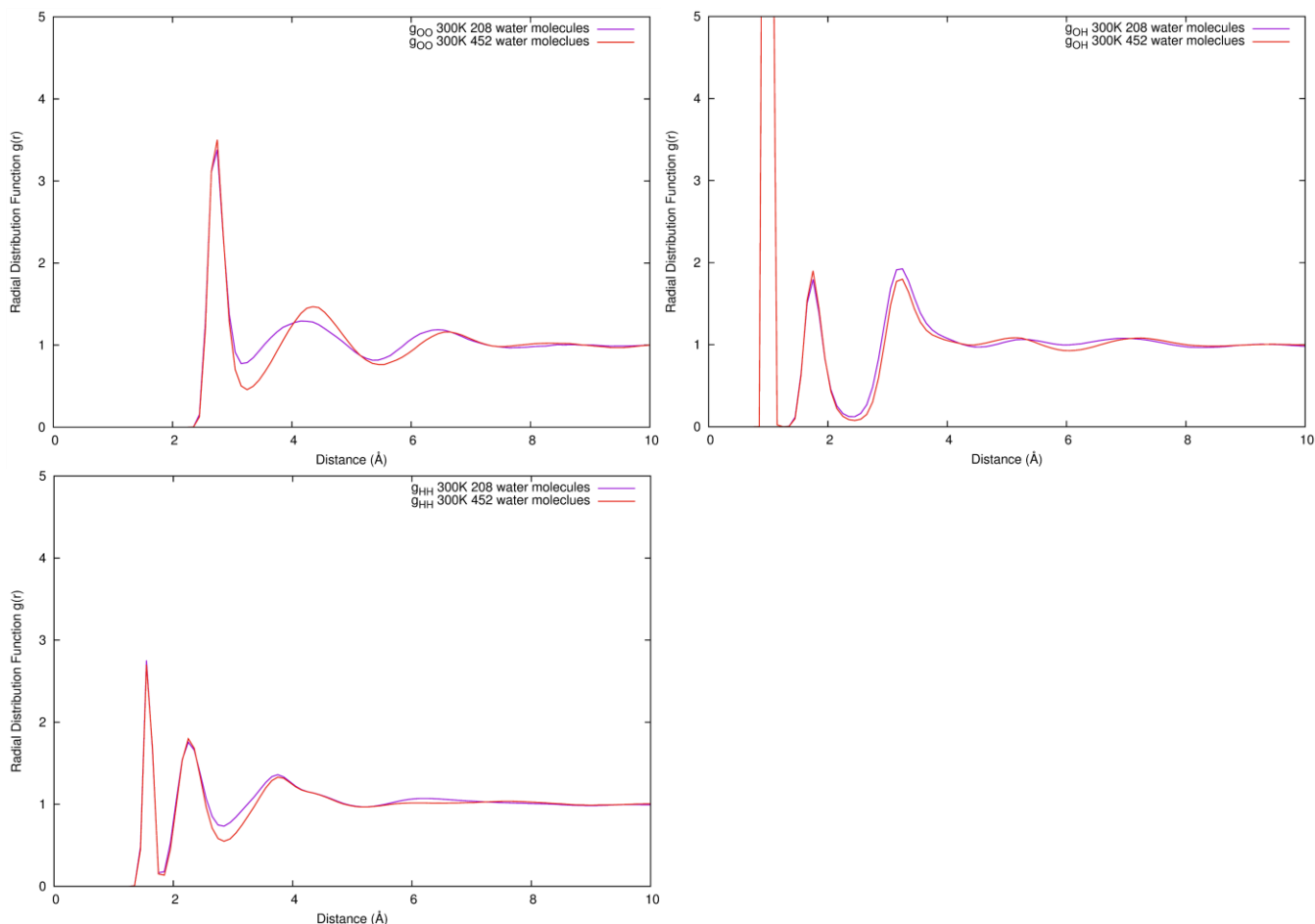


Figure S50. Radial distribution function (RDF) of the solvent water molecules in the simulation box of the neutral cubane.

Table S11. Different functionals (BP86,^{14, 15} PBE,⁵ TPSS,¹⁶ BLYP^{14, 17}) and dispersion correction models such as Grimme's D3,⁹ D3_c9 (three-body-terms⁹) and the non-local correction rvv10¹⁸ were used to optimize the structure of the cubane (**Co₄O₄-dpk**) *in vacuo*. Co-Co distances given in Å in Table S11 were compared with the experimental values from single crystal X-ray structure determination (Table S2). The best agreement with experimental data was found for PBE-D3 where deviations from the experiment were always smaller than 0.1 Å.

Bond	BP86-D3	PBE-D3	PBE-rvv10	PBE-D3_c9	TPSS-D3	BLYP-D3	Exp.
Co1-Co1a	3.27	3.21	3.27	3.28	3.19	3.29	3.16
Co1-Co2	3.27	3.24	3.27	3.28	3.19	3.30	3.21
Co1-Co2a	3.33	3.30	3.33	3.35	3.30	3.40	3.30
Co1a-Co2	3.36	3.32	3.36	3.33	3.26	3.38	3.30
Co1a-Co2a	3.17	3.14	3.17	3.17	3.11	3.24	3.21
Co2-Co2a	3.15	3.11	3.13	3.18	3.20	3.19	3.07

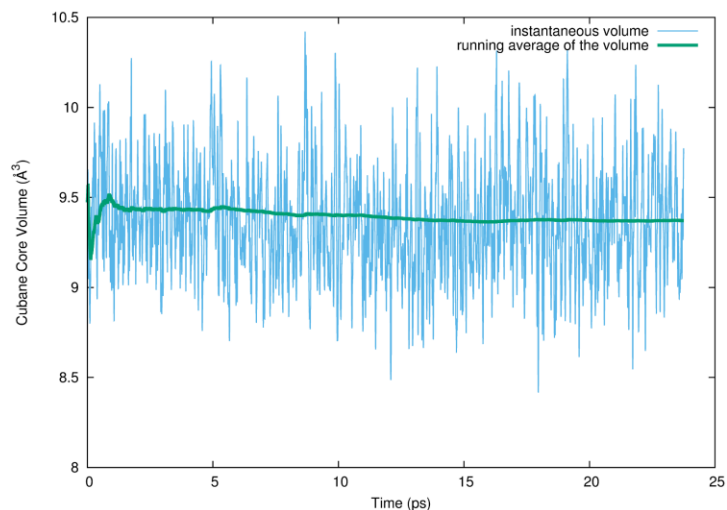


Figure S51. Evolution of volume enclosed by the cubane cage of **Co₄O₄-dpk** during the DFT-MD run including 208 solvent water molecules.

- (1) VandeVondele, J.; Krack, M.; Mohamed, F.; Parrinello, M.; Chassaing, T.; Hutter, J. *Comput. Phys. Comm.* **2005**, *167*, 103.
- (2) CP2K Development Group.
- (3) Bussi, G.; Donadio, D.; Parrinello, M. *J. Chem. Phys.* **2007**, *126*, 14101.
- (4) Blumberger, J.; Bernasconi, L.; Tavernelli, I.; Vuilleumier, R.; Sprik, M. *J. Am. Chem. Soc.* **2004**, *126*, 3928.
- (5) Perdew, J. P.; Ernzerhof, M.; Burke, K. *J. Chem. Phys.* **1996**, *105*, 9982.
- (6) VandeVondele, J.; Hutter, J. *J. Chem. Phys.* **2007**, *127*, 114105.
- (7) Hartwigsen, C.; Goedecker, S.; Hutter, J. *Phys. Rev. B* **1998**, *58*, 3641.
- (8) Goedecker, S.; Teter, M.; Hutter, J. *Phys. Rev. B* **1996**, *54*, 1703.
- (9) Grimme, S.; Antony, J.; Ehrlich, S.; Krieg, H. *J. Chem. Phys.* **2010**, *132*, 154104.
- (10) Tkatchenko, A.; Scheffler, M. *Phys. Rev. Lett.* **2009**, *102*, 73005.
- (11) DiStasio, R. A., JR; Santra, B.; Li, Z.; Wu, X.; Car, R. *J. Chem. Phys.* **2014**, *141*, 84502.
- (12) Skinner, L. B.; Huang, C.; Schlesinger, D.; Pettersson, L. G. M.; Nilsson, A.; Benmore, C. J. *J. Chem. Phys.* **2013**, *138*, 74506.
- (13) Soper, A. K.; Benmore, C. J. *Phys. Rev. Lett.* **2008**, *101*, 65502.
- (14) Becke, A. D. *Phys. Rev. A* **1988**, *38*, 3098.
- (15) Perdew, J. P. *Phys. Rev. B* **1986**, *33*, 8822.
- (16) Tao, J.; Perdew, J. P.; Staroverov, V. N.; Scuseria, G. E. *Phys. Rev. Lett.* **2003**, *91*, 146401.
- (17) Chengteh Lee; Weitao Yang; and Robert G. Parr. *Phys. Rev. B* **1988**, *37*, 785.
- (18) Sabatini, R.; Gorni, T.; Gironcoli, S. de. *Phys. Rev. B* **2013**, *87*, 041108.

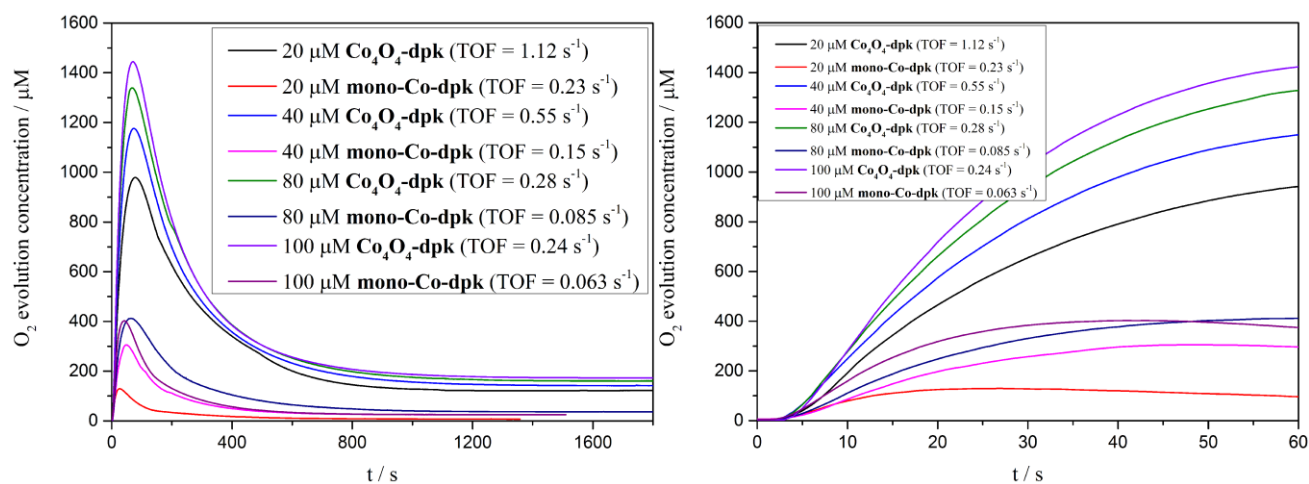


Figure S52. Clark electrode kinetics of visible light-driven water oxidation catalyzed by 20, 40, 80, and 100 μM Co₄O₄-dpk and mono-Co-dpk, respectively. TOF calculations of 20, 40, and 80, and 100 μM WOC catalyzed water oxidation are based on time intervals of 27, 49, and 60 s, respectively.

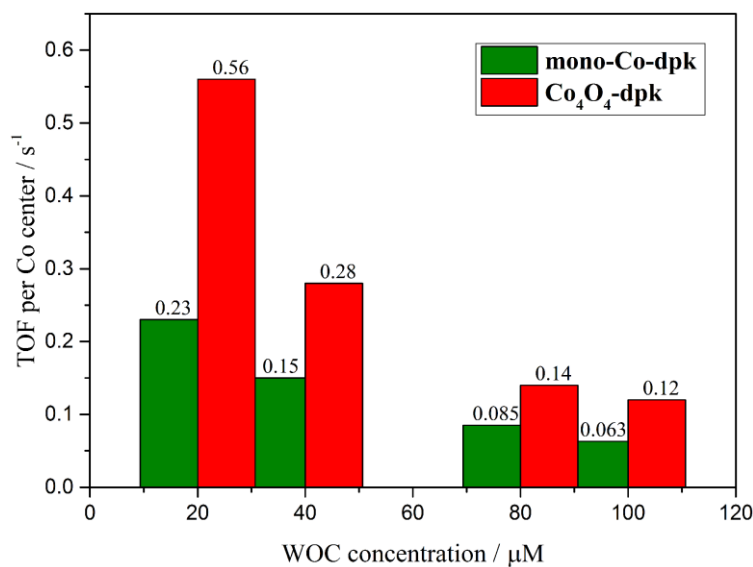


Figure S53. TOF per Co center of the above water oxidation kinetics with 20, 40, 80, and 100 μM WOC, respectively (calculation of TOF per Co center of Co₄O₄-dpk based on the edge-site).

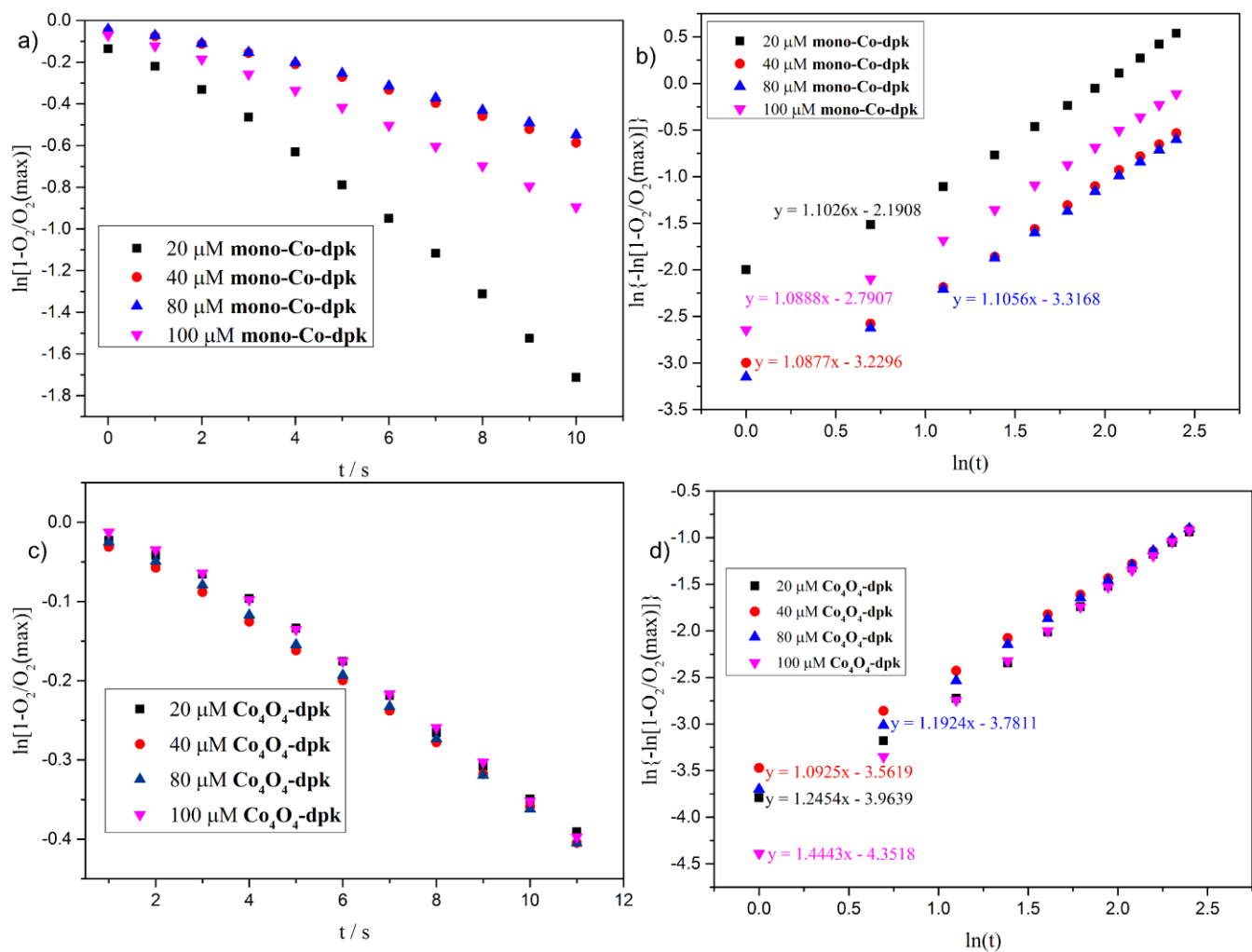


Figure S54. Tentative evaluation of mono-Co₄O₄-dpk (a, b) and Co₄O₄-dpk (c, d) for first order kinetics.